Evolutionary origin and functional mechanism of Lhcx in the diatom photoprotection

Running head: Evolutionary origin and mechanism of diatom Lhcx

Minoru Kumazawa[1,2], Seiji Akimoto[3], Atsushi Takabayashi[2], Ko Imaizumi[1], Shoko Tsuji[1], Hazuki Hasegawa[4], Atsushi Sakurai[4], Sousuke Imamura[4], Noriko Ishikawa[1], Natsuko Inoue-Kashino[5], Yasuhiro Kashino[5] & Kentaro Ifuku[1]

[1]Graduate School of Agriculture, Kyoto University, Japan

[2]Institute of Low Temperature Science, Hokkaido University, Japan

[3]Graduate School of Science, Kobe University, Japan

[4]Space Environment and Energy Laboratories, NTT, Inc., Japan

[5]Graduate School of Science, University of Hyogo, Japan

The author responsible for the distribution of materials integral to the findings presented in this article, in accordance with the policy described in the Instructions for Authors, is Dr. Kentaro Ifuku (ifuku.kentaro.2m@kyoto-u.ac.jp).

Summary

Diatoms are red-lineage algae that utilize the light-harvesting complex (LHC) subfamily Lhcx for photoprotection via non-photochemical quenching (NPQ); however, its evolutionary origin and molecular mechanism remain poorly understood. Through molecular phylogenetic analysis, we show that diatom Lhcxs and green algal Lhcsrs evolved from a common ancestor, with green plants subsequently acquiring them via horizontal gene transfer. To investigate the functional role of Lhcx1, we generated knockout mutants of *Chaetoceros gracilis*, a diatom with low Lhcx redundancy. The *lhcx1* mutants nearly abolished NPQ, and time-resolved fluorescence measurements revealed that Lhcx1-mediated quenching occurs in energetically detached antenna complexes. Clear-native PAGE with Amphipol further indicated that CgLhcx1 interacts with the FCP L-dimer, functioning as a peripheral antenna for the $C_2S_2M_2$ PSII–FCPII supercomplex. Notably, under high-light acclimation, *lhcx1* mutants exhibited higher PSII effective quantum yields than wild type, attributable to reduced antenna size and enhanced carbon fixation capacity. The absence of NPQ accelerated high-light acclimation and was accompanied by increased xanthophyll accumulation, indicating that compensatory mechanisms can enhance overall photosynthetic efficiency. Together, these findings reveal the evolutionary origin of Lhcx/Lhcsr proteins and define the molecular basis of Lhcx1-mediated photoprotection in diatoms, providing fundamental insights into LHC-based photoprotection across photosynthetic lineages.

Introduction

Photosynthesis consists of photochemical reactions in which two photosystems connected in series convert light energy into chemical energy. Among photosynthetic organisms, red-lineage secondary endosymbiotic algae, which possess plastids derived from red algae acquired through cellular endosymbiosis, are widely adapted to aquatic environments on Earth (Pierella Karlusich et al., 2020; Pierella Karlusich et al., 2025). Light conditions in these environments are as dynamic as those in terrestrial environments, making it extremely important for photosynthetic organisms to protect their photosystems from excess light to suppress the generation of harmful reactive oxygen species caused by the absorption of excessive light energy. Non-Photochemical Quenching (NPQ), which dissipates excess light energy as heat, plays a crucial role in this protective mechanism (Niyogi, 2000).

Multiple NPQ mechanisms with different induction times exist, and these exhibit distinct characteristics depending on the taxonomic group (Goss and Lepetit, 2015; Malnoë, 2018). In particular, energy-dependent quenching (qE) is a major component of NPQ and is carried out by Light-Harvesting Complex (LHC) proteins (Peers et al., 2009; Goss and Lepetit, 2015; Buck et al., 2019). In red-lineage secondary endosymbiotic algae including diatoms, qE depends on the Lhcx subfamily of the LHC family (Buck et al., 2019; Croteau et al., 2025). The diatom LHC is called FCP (Fucoxanthin-Chlorophyll *a*/*c*-binding Protein) because it binds pigments such as Chl *c*, fucoxanthin, diadinoxanthin, and diatoxanthin in addition to Chl *a*. In addition to Lhcx, xanthophyll cycle pigments play a crucial role in qE induction. In diatoms, the proton gradient (ΔpH) across the thylakoid membrane activates the diadinoxanthin to diatoxanthin converting cycle (Ddx-Dtx cycle) (Lavaud and Kroth, 2006; Goss and Lepetit, 2015). The violaxanthin-antheraxanthin-zeaxanthin (VAZ) cycle, well known in land plants (Niyogi et al., 1998), also functions in diatoms, complementing the Ddx-Dtx cycle (Lohr and Wilhelm, 1999; Giossi et al., 2025). Green algae, on the other hand, utilize qE dependent on the Lhcsr subfamily, which is homologous to Lhcx, as well as state transitions (qT),

where LHCII detaches from photosystem II (PSII) and binds to photosystem I (PSI) through phosphorylation control to adjust the excitation balance between the two photosystems (Allorent et al., 2013; Minagawa and Tokutsu, 2015). Despite the well-established sequence homology between Lhcx and Lhcsr, these proteins exhibit differences in their regulatory mechanisms at the gene expression level (Allorent et al., 2016; Petroutsos et al., 2016; Tokutsu et al., 2019a; Tokutsu et al., 2019b; Im et al., 2024; Zhang et al., 2024). Furthermore, while land plants require PsbS for qE induction (Li et al., 2000; Niyogi, 2004), diatoms lack this protein. The evolutionary origin of Lhcx/Lhcsr has not been extensively discussed due to the lack of comprehensive phylogenetic analyses of LHC subfamilies.

NPQ in red-lineage algae has been studied in diatoms and *Nannochloropsis* belonging to heterokont algae (Bailleul et al., 2010; Buck et al., 2019; Park et al., 2019; Buck et al., 2021; Giovagnetti et al., 2022). In model diatom species, multiple Lhcx isoforms are expressed under different conditions and show functional redundancy. Therefore, almost complete Lhcx-deficient strains have not been created in diatoms to date, and the physiological responses and details of excitation energy transfer in states with significantly deficient NPQ have not been fully elucidated. In contrast, *Chaetoceros gracilis* has low redundancy of Lhcxs, with primarily only CgLhcx1 being expressed (Kumazawa et al., 2022), providing the possibility that an almost complete Lhcx-deficient strain can be obtained by creating a knockout of this CgLhcx1. Furthermore, the three-dimensional structures of PSII–FCPII (Nagao et al., 2019; Wang et al., 2019; Nagao et al., 2022) and PSI–FCPI (Nagao et al., 2020a; Xu et al., 2020) supercomplexes have already been elucidated in this species, establishing a foundation for structural biology research. This study aims to investigate the origin of Lhcx phylogenetically and to elucidate the mechanism of its excitation energy quenching for high light (HL) protection by creating Lhcx1-deficient mutants in *C. gracilis* using CRISPR/Cas9 genome editing technology.

Results

Origin of LHCs in the Lhcx/Lhcsr Subfamily

To elucidate the origins of the diatom Lhcx and green algal Lhcsr subfamilies, which perform NPQ, we conducted a comprehensive molecular phylogenetic analysis of light-harvesting complexes (LHCs) from red algae, green algae, cryptophytes, and diatoms, and represented the estimated phylogenetic tree as an unrooted tree (Figure 1). Comprehensive retrieval of LHC sequences by BLAST confirmed that, as in our previous reports, red algae possess only the Lhcr subfamily, cryptophytes have Lhcr and Lhcz subfamilies, and green algae contain Lhca, Lhcb, and Lhcsr subfamilies, while diatoms possess Lhcr, Lhcz, Lhcq, CgLhcr9 homolog, Lhcx, and Lhcf subfamilies (Kumazawa et al., 2022; Kumazawa and Ifuku, 2024). In Figure 1, each LHC subfamily in the red lineage is separated. However, within the Lhcr subfamily, there exists diversity among the Lhcr proteins from red algae, cryptophytes, and diatoms, encompassing gene groups with distant evolutionary relationships.

Lhcx and Lhcsr formed a monophyletic clade with an ultrafast bootstrap value of 100% (Figure 1, inset). Within this clade, *Thalassiosira pseudonana* Lhcx6_1 and *Cyclotella cryptica* Lhcx6_1, derived from diatoms belonging to the order Thalassiosirales, clearly branched at the most basal position and were evolutionarily distant from typical Lhcx and Lhcsr proteins. All Lhcx1–3 proteins from the diatom *Chaetoceros gracilis* were positioned within the typical Lhcx clade. Additionally, the Lhcx and Lhcsr clade showed monophyly with the Lhcq, CgLhcr9 homolog, and Lhcf subfamilies, supported by a high bootstrap value (100%). Within that clade, Lhcq was located at the most basal position, while the Lhcx/Lhcsr clade was positioned internally. In contrast, the Lhcx/Lhcsr clade did not show monophyly with the Lhca/Lhcb clade. Furthermore, the Lhcr of red algae and the Lhca and Lhcb subfamilies, which are responsible for light harvesting in red and green algae possessing primary plastids, did not form a monophyletic group; between them existed cryptophyte Lhcr, diatom Lhcr,

106 cryptophyte and diatom Lhcz, as well as other subfamilies of the red evolutionary lineage. These data
107 suggest that Lhcsr and Lhcx subfamilies are derived from the red-lineage specific subfamilies.
108

109 **Creating *Lhcx1* Knockout Strains with Ribozyme-Based Genome Editing**

110 *C. gracilis* has three typical Lhcx genes (*CgLhcx1–3*): according to the genome database of *C.*
111 *gracilis* (ChaetoBase v1.1, https://chaetoceros.nibb.ac.jp/), *CgLhcx1* showed the highest transcription
112 level by a significant margin (Kumazawa et al., 2022). Therefore, we decided to create an *Lhcx1*-
113 deficient mutant in *C. gracilis* using the CRISPR/Cas9 system. To facilitate the comprehensive
114 analysis of LHC genes using genome-editing in *C. gracilis,* we have developed the inducible
115 CRISPR/Cas9 system, in which both Cas9 and guide RNA (gRNA) expression is regulated by the
116 inducible Pol-II-type promoter. First, we introduced the *Cas9* gene under the nitrate reductase (NR)
117 promoter into wild-type *C. gracilis* with a vector having the nourseothricin resistance gene (*nat*) via
118 electroporation (Supplemental Figure 1A, B). Colonies obtained through antibiotic-resistance
119 selection were further selected for high Cas9 expression in the presence of nitrate by immunoblotting
120 (Supplemental Figure 1B). The selected hC9_5 strain showed morphology and growth characteristics
121 equivalent to the wild-type strain (WT) and was established as the host strain for the genome editing
122 (Supplemental Figure 1C, D). Second, to express mature gRNA in the host hC9_5 under the NR
123 promoter, we employed a method utilizing ribozymes (Gao and Zhao, 2014; Zhang et al., 2017;
124 Taparia et al., 2022). This method employed a Ribozyme-gRNA-Ribozyme (RGR) construct in which
125 a hammerhead ribozyme with self-cleavage activity at the 3' end was attached to the 5' end of the
126 gRNA, and an HDV ribozyme with self-cleavage activity at the 5' end was attached to the 3' end of
127 the gRNA. This RGR cassette for the gene of interest can be easily constructed by overlap PCR and
128 inserted into pCgNRp^{ble} vector, having an antibiotic-resistant gene against zeocin (*ble*) for the second
129 selection.

130 The transformation of the host hC9_5 strain with the linearized pCgNRp^{ble}-Lhcx1-RGR vector
131 produced 252 zeocin-resistant colonies, from which 23 strains were randomly selected and 13 strains
132 had various mutations in the target sequence of the *CgLhcx1* gene (Supplemental Figure 2A, B, C).
133 Among the strains confirmed for target sequence editing, *lhcx1-7*, *15*, and *234* strains were used for
134 subsequent analysis. When the nucleotide sequences of the *Lhcx1* region were confirmed by Sanger
135 sequencing, heterogeneity was observed (Supplemental Figure 2C). Since *C. gracilis* is a diploid
136 organism like other diatoms, mutagenic events can occur in both alleles to completely inactivate the
137 target gene. However, simultaneous mutations in both alleles are rare, and in most cases only one allele
138 is mutated or neutral mutations such as in-frame deletions/insertions may occur, resulting in the
139 formation of mixed cell populations with different mutation status and types through subsequent cell
140 divisions (Huang and Daboussi, 2017). Therefore, we examined the accumulation of Lhcx1 protein in
141 these strains by western blotting using an anti-Lhcx1 antibody (Supplemental Figure 2D). Almost no
142 accumulation of Lhcx1 protein was observed in the *lhcx1-7* and *lhcx1-15* strains. On the other hand,
143 the *lhcx1-234* strain showed reduced accumulation of Lhcx1 compared to WT, but it was not a
144 complete deficiency since *lhcx1-234* may include neutral mutations such as in-frame
145 deletions/insertions.
146
147 **Phenotypic Analysis of *Lhcx1* Deficient Strains**
148 WT and *lhcx1-7*, *15*, and *234* strains were cultured with air bubbling for 7–8 days under low light
149 (LL) at 30 μmol photons m^{-2} s^{-1} and high light (HL) at 300 μmol photons m^{-2} s^{-1}. We selected 300
150 μmol photons m^{-2} s^{-1} as high light because it is still much higher than the light intensity at the deep
151 chlorophyll maximum layer, where diatoms are typically most abundant. No significant differences in
152 growth were observed between WT and genome-edited strains (Supplemental Figure 3). To investigate
153 the photosynthetic characteristics of WT and *lhcx1* strains, pulse-amplified modulated (PAM)

154 fluorescence measurements were performed on day 3 and day 7–8 using cells cultured under LL and
155 HL conditions (Figure 2, Supplemental Figure 4). As a result, *lhcx1-7*, *15*, and *234* were hardly able
156 to induce NPQ, an indicator of thermal dissipation of excess excitation energy around PSII, under both
157 LL and HL conditions (Figure 2A, Supplemental Figure 4A). The *lhcx1* strains cultured under LL
158 showed lower photochemical quenching qP under light exposure compared to WT, indicating a more
159 reduced state of the plastquinone pool. However, this trend was not clear in the *lhcx1* strains cultured
160 under HL, because non-regulated energy dissipation due to photoinhibition affects the qP level (Figure
161 2B). The effective quantum yield of PSII, Y(II), showed higher values in all *lhcx1* strains compared to
162 the WT strain in cells cultured under HL for 7–8 days (Figure 2C). In cells cultured under HL for 3
163 days, *lhcx1* strains showed a trend of higher Y(II) compared to WT, but the difference was not
164 significant (Supplemental Figure 4C). The *lhcx1-7, 15* strains exhibited significantly higher oxygen-
165 evolving activity compared to WT cells at the same total Chl *a* content of 5 μg (Figure 3). The *lhcx1-*
166 *234* strains showed the tendency towards higher oxygen-evolving activity, though it was not
167 statistically significant (p = 0.157). This may be due to the mosaic genetic background of *Lhcx1*
168 mutations in *lhcx1-234*.
169

170 **Whole-Cell Absorption Spectra and Pigment Analysis**

171 The whole-cell absorption spectra showed no significant differences between WT and *lhcx1*
172 mutants in cells cultured under LL, while in the cells cultured under HL, the *lhcx1* mutants exhibited
173 greater absorption in the 400–500 nm region compared to the WT (Supplemental Figure 5). Since this
174 region corresponds to carotenoid absorption, pigment analysis using HPLC (High Performance Liquid
175 Chromatography) was performed to examine carotenoid contents. The amount of Chl *a* per cell was
176 decreased in the mutants compared to WT under LL conditions (Figure 4A). Additionally, under HL
177 conditions, WT also showed a decrease in Chl *a* content compared to LL conditions, but the decrease

178 tends to be greater in the *lhcx1* mutants. Since the total absorption spectra were normalized at the Qy
179 peak of Chl *a*, carotenoid content was quantified per Chl *a* amount. Fucoxanthin, the major carotenoid
180 in *C. gracilis* FCP, showed no significant differences between WT and mutants under both light
181 conditions, except for *lhcx1-15* under HL conditions (Figure 4B). The *lhcx1-15* under HL conditions
182 showed slightly lower fucoxanthin content compared to WT under the same conditions. On the other
183 hand, for diadinoxanthin (Ddx) and diatoxanthin (Dtx), the major pigments of the diatom xanthophyll
184 cycle, no significant differences in accumulation were observed between WT and *lhcx1* mutants under
185 LL conditions (Figure 4C, D). In contrast, under HL conditions, WT showed greater accumulation of
186 Dtx compared to LL conditions. The mutant strains accumulated significantly more Dtx compared to
187 the WT under the same conditions. Regarding Ddx, both WT and mutants showed greater
188 accumulation under HL conditions compared to LL conditions, but significant increases in
189 accumulation in mutants compared to WT were not observed, except for *lhcx1-15*. Total xanthophyll
190 cycle pigments (Ddx+Dtx) were also increased in *lhcx1* mutants under HL (Figure 4E). The de-
191 epoxidation state (DEPS = [Dtx]/([Dtx]+[Ddx])), an indicator of the xanthophyll cycle, was calculated
192 from the accumulation of Dtx and Ddx (Figure 4F). Under LL, there was no significant difference
193 between WT and mutants. Under HL, the WT showed a higher DEPS (0.34) compared to LL
194 conditions. The mutants showed significantly higher DEPS (0.47–0.52) compared to WT under the
195 same conditions.
196
197 **Steady-State Low-Temperature Fluorescence and Antenna Size Measurements**
198 WT and *lhcx1* cultured under HL were subjected to 30-minute treatments under either dark
199 conditions (dark-treated) or HL conditions (HL-treated), then were immediately frozen in liquid
200 nitrogen, and used for the low-temperature (77K) fluorescence spectra measurements (Figure 5A, B).
201 WT was measured as two independent samples cultured separately (solid and dashed lines in Figure

202 5A, B). The 77K steady-state fluorescence spectra well represent the distribution of excitation energy
203 between photosystems and light-harvesting pigment proteins. The excitation wavelength was 459 nm,
204 which efficiently excites Chl *c* and fucoxanthin bound to the peripheral antenna FCP in diatoms. The
205 77K fluorescence spectra of *C. gracilis* showed two peaks derived from CP43 and CP47 of
206 photosystem II, observed around 686 nm and 694 nm, respectively (Andrizhiyevskaya et al., 2005;
207 Nagao et al., 2010). In all cells cultured under HL, the mutants showed lower CP43 peaks compared
208 to the WT in spectra normalized at the CP47 peak (Figure 5A). The fluorescence intensity around 680
209 nm, which is considered to be the fluorescence from FCP, was smaller in *lhcx1* mutants under dark
210 conditions compared to the WT. These indicate that energy transfer from the peripheral antenna FCP
211 via CP43 is prominent in the dark especially in WT. This also suggests that the effective antenna size
212 of PSII differed between WT and *lhcx1* in the dark. Therefore, the antenna size after dark adaptation
213 of cells cultured under HL was measured by measuring the induction curve of Chl fluorescence with
214 a Fluorometer FL 3500 (PSI, Czech Republic) (Nedbal et al., 1999). As a result, it was revealed that
215 *lhcx1* had a significantly smaller effective antenna size of PSII compared to WT in all strains
216 (Supplemental Figure 6).
217
218 **Time-Resolved Low-Temperature Fluorescence Spectra**
219 To elucidate the process of excitation energy transfer from the peripheral antenna FCP to the
220 photosystems, time-resolved fluorescence (TRF) spectra were measured under the same conditions as
221 the samples subjected to low-temperature steady-state fluorescence spectrum measurements. TRF
222 fluorescence was measured on samples of whole cells that were frozen in liquid nitrogen immediately
223 after dark treatment and HL treatment (300 μmol photons m^{-2} s^{-1}). This allows observation of
224 excitation energy transfer and quenching in states where NPQ is not induced and where it is induced
225 (Chukhutsina et al., 2017). Fluorescence decay-associated spectra (FDAS) were obtained by global

226 analysis that decomposed the obtained TRF spectra into multiple exponential components with time
227 as a variable (Figure 6, Supplemental Figure 7). In FDAS, positive peaks (decay) indicate the decay
228 of fluorescence, while negative peaks (rise) indicate the rise of fluorescence. From the TRF spectra of
229 the WT, FDAS were constructed with six-time constants. The assignment of each peak followed
230 previous literature (Andrizhiyevskaya et al., 2005; Nagao et al., 2010). In the dark-adapted WT, the
231 FDAS with a lifetime of 40 ps showed positive peaks of FCP at <680 nm and a large negative peak
232 around 687 nm corresponding to CP43 (black solid line in Figure 6 and Supplemental Figure 7). This
233 reflects excitation energy transfer from FCP to CP43. In the spectrum of the second lifetime of 140 ps,
234 positive peaks were observed not only at ~680 nm but also around 687 nm corresponding to CP43,
235 while the waveform around 694 nm corresponding to CP47 showed a convex downward shape. This
236 is thought to be due to the negative peak of CP47 overlapping with the shoulder of the nearby positive
237 peak of CP43, and is considered to indicate excitation energy transfer from FCP/CP43 to CP47. Also,
238 in the second lifetime component, a PSI positive peak at ~710 nm was observed, which, together with
239 the negative peak of FCP, indicates the excitation energy transfer from FCP to PSI. The third lifetime
240 of 640 ps continued to show the same trend as 140 ps, suggesting that excitation energy transfer from
241 FCP/CP43 to CP47 was ongoing. The fourth and fifth lifetimes, at 1.6 ns and 3.8 ns, showed positive
242 peaks corresponding to CP43 and CP47, indicating simple fluorescence decay. The longest lifetime of
243 26 ns did not exhibit a prominent positive peak around 710 nm, which is characteristic of PSI
244 fluorescence, but instead showed positive peaks corresponding to CP43 and CP47, associated with
245 charge recombination in photosystem II. Therefore, excitation energy transfer from PSII to PSI, so-
246 called spillover, did not occur.
247 On the other hand, WT subjected to HL (black dashed line in Figure 6 and Supplemental Figure 7)
248 showed a similar waveform at 40 ps as the dark-adapted WT. At 140 ps, although the positive peak
249 around 687 nm was much larger compared to the dark-adapted WT, the value at the dip around 694

250 nm was larger than that of the dark-adapted WT. In other words, WT acclimated to HL had a smaller
251 fluorescence rise at CP47 compared to the dark-adapted sample, while the energy decay around 687
252 nm was larger. The *lhcx1* mutant, which does not induce NPQ, showed spectra similar to the dark-
253 adapted WT in the first- and second-time constants when dark-adapted (blue, green, and red solid lines
254 in Figure 6 and Supplemental Figure 7A, B). However, in the third time constant (640 ps), while the
255 dark-adapted WT showed excitation energy transfer from FCP/CP43 to CP47, *lhcx1* already showed
256 positive peaks at both 687 nm and 694 nm, indicating fluorescence decay of CP43 and CP47. In
257 subsequent time constants, 687 nm and 694 nm also showed only positive peaks. The HL-acclimated
258 *lhcx1* (blue, green and red dashed line in Figure 6 and Supplemental Figure 7A, B) also showed spectra
259 similar to the dark-adapted *lhcx1* at all time constants and did not show the large positive peak around
260 687 nm at 140 ps observed in the HL-acclimated WT. Furthermore, since energy transfer from FCPII
261 to CP43 and CP47, and from CP43 to CP47 was completed by 140 ps, similar to the HL-treated WT
262 and dark-treated *lhcx1*, it was concluded that *lhcx1* has a smaller antenna size compared to the WT
263 even under HL conditions. From the above, while the decay of fluorescence around 687 nm is normally
264 attributed to energy transfer from CP43, when looking at the energy transfer of *lhcx1* at the same time
265 constant, such decay is not observed. Therefore, it is concluded that the decay of fluorescence around
266 687 nm in the HL-acclimated WT is not decay of CP43 but quenching attributed to Lhcx1.
267

268 **Molecular interaction of Lhcx1 in thylakoid membranes**

269 To determine the localization of Lhcx, we performed native-PAGE followed by second-dimension
270 SDS-PAGE and subsequent immunoblotting using anti-Lhcx1 antibody. Since conventional Clear
271 Native (CN)-PAGE with deoxycholate made it difficult to separate diatom $C_2S_2M_2$ (Core$_2$–S-
272 tetramer$_2$–M-tetramer$_2$) PSII–FCPII while keeping FCP-A (which contains CgLhcf1 as a major
273 component) bound to PSII (Nagao et al., 2012), we applied a modified CN-PAGE using Amphipol

274 A8-35 (Kameo et al., 2021), which enhances the stability of solubilized protein complexes, instead of
275 deoxycholate as the surfactant that imparts negative charge to proteins (Figure 7A). In the diatom *C.*
276 *gracilis*, a dense band was observed at a higher molecular weight position than spinach $C_2S_2M_2$
277 ($Core_2$–S-$trimer_2$–M-$trimer_2$) PSII–LHCII. Additionally, a broad brown band, which was observed at
278 a higher molecular weight position than the LHC/FCP monomer, extended to a lower molecular weight
279 position than the spinach LHCII trimer. This CN-PAGE gel strip was subjected to SDS-PAGE with a
280 gel containing 6 mol L^{-1} urea to separate each subunit (Figure 7B). Annotation of each spot was based
281 on previous reports (Nagao et al., 2007; Zhou et al., 2024). The amino-acid sequence of
282 HGRIAQLAFLGN shared with CgLhcf2 and CgLhcf12 was identified from the major FCP fraction
283 (Ishihara et al., 2015). These reports indicate that FCP-B/C is one of the major FCPs in *C. gracilis*.
284 Furthermore, since the FCP-B/C heterodimer is presumed to be loosely bound to $C_2S_2M_2$ PSII–FCPII
285 and transfer excitation energy, it was designated as L (Loose)-dimer (Figure 7A, B). The thylakoid
286 membranes of *lhcx1* were also subjected to CN-PAGE (Supplemental Figure YYY). While *lhcx1* has
287 the $C_2S_2M_2$ PSII–FCPII as well as WT, *lhcx1* has a slightly paler broad band of L-dimers. Additionally,
288 immunoblotting was performed to identify the Lhcx1 spot from the spots in the two-dimensional SDS-
289 PAGE (Figure 7C). The Lhcx1 spot, indicated by the blue arrowhead in Figure 7C, was detected at a
290 higher molecular weight than FCP-B/C in 2D-SDS-PAGE. In the 1D-CN-PAGE direction, the spot of
291 Lhcx1 was detected across a wide range of multimers from monomers to higher-order multimeric
292 complexes, co-migrating with FCP-B/C (Figure 7B). That spot of Lhcx1 in 2D-PAGE with oriole stain
293 is paler than FCP-A/B/C because of lower accumulation of Lhcx1 than FCP-A/B/C. This result
294 suggests that Lhcx1 may interact with the FCP-B/C dimers, which function as the loosely associated
295 antenna of $C_2S_2M_2$ PSII–FCPII.
296

297 **Phenotype of *lhcx1* Mutants in High CO_2 Environment**

298 We investigated whether the *lhcx1* mutants, which showed a higher effective quantum yield of PSII
299 when acclimated to HL under normal atmospheric aeration conditions, would further improve their
300 PSII effective quantum yield by enhancing downstream electron sink capacity with 3% CO_2 addition.
301 First, even when cultured with CO_2 aeration, *lhcx1* showed almost no NPQ regardless of light intensity
302 (Supplemental Figure 9A). The effective quantum yield of PSII, Y(II), increased in *lhcx1* when
303 cultured with CO_2 aeration even under LL conditions, where no difference was observed with
304 atmospheric aeration (solid line in Supplemental Figure 9C). This Y(II) under light irradiation
305 increased with time during the initial irradiation period and reached a constant value after about 2
306 minutes, which is thought to be due to the activation of the carbon assimilation pathway. Additionally,
307 an increase in Y(II) was also observed under HL conditions. Photochemical quenching qP, which
308 indicates the redox state of plastoquinone, was similar between WT and *lhcx1* under LL conditions.
309 As observed in Figure 2B, qP of *lhcx1* varied among strains, with strains having lower Y(II) showing
310 lower qP under HL conditions (Supplemental Figure 9B).

311 To understand the general physiological response of *lhcx1*, we performed RNA sequencing analysis
312 under LL/HL and ambient/3%-CO_2-supplemented air conditions. Under ambient air conditions, HL
313 treatment induced 1,494 genes in WT and 1,530 genes in *lhcx1* mutant, with 458 genes commonly
314 upregulated in both genotypes. Under CO_2-enriched conditions, HL induced substantially more genes:
315 2,411 in WT and 2,402 in *lhcx1* mutant. To identify responses compensating the absence of NPQ in
316 *lhcx1*, we compared the magnitude of HL response (fold-change from LL to HL) between genotypes.
317 *lhcx1* showed enhanced HL response compared to WT in 978 genes under ambient air and 311 genes
318 under CO_2-enriched conditions, with 105 genes showing this enhanced response under both ambient
319 and CO_2 conditions. KEGG pathway enrichment analysis reveals that while both WT and *lhcx1*
320 respond to HL through porphyrin metabolism and photosynthesis pathways (Figure 8A), *lhcx1* mutant

321 specifically enhances carbon fixation and central carbon metabolism pathways under both ambient air

322 and CO_2 conditions (Figure 8B).

323 **Discussions**

324 The deficiency of Lhcx, while Lhcx belongs to the LHC family primarily responsible for light
325 harvesting, almost completely suppresses the induction of non-photochemical quenching (NPQ). The
326 NPQ-deficient *lhcx1* strains acclimated by inducing various HL defense systems possessed by *C.*
327 *gracilis* and showed higher PSII activity compared to the WT. Since the increase in PSII activity was
328 also induced in *lhcx1* with the addition of CO_2, it was revealed that acclimation of downstream electron
329 sinks in the electron transport chain, along with acclimation of the upstream light-harvesting system,
330 plays an important role in HL acclimation of *C. gracilis*. This study suggests that the multiple
331 photoprotection mechanisms can be interrelated and flexibly regulated in response to environmental
332 changes in the marine diatom *C. gracilis*.

333

334 **Origin of Lhcx**

335 The Lhcx subfamily, which is responsible for non-photochemical quenching (NPQ) in red-lineage
336 secondary endosymbiotic algae such as heterokonts including diatoms, and presumably haptophytes,
337 and the Lhcsr subfamily, which similarly mediates NPQ in green algae, streptophyte algae, and
338 bryophytes, have been considered to share a common ancestral gene as they form a monophyletic
339 group (Koziol et al., 2007). Although the Lhcx/Lhcsr subfamily is suggested to be derived from the
340 red lineage, detailed molecular phylogenetic relationships with other subfamilies have not been
341 thoroughly investigated, likely due to insufficient sequence information (Dittami et al., 2010). In this
342 study as well, the diatom Lhcx subfamily and the basal streptophyte algae and core green algae Lhcsr
343 subfamily formed a monophyletic group (Figure 1). The Lhcx/Lhcsr clade formed by these showed
344 strong support for monophyly with the diatom Lhcq, CgLhcr9 homolog, and Lhcf subfamilies, and
345 was in a different clade from the green algae Lhca/Lhcb subfamily, clearly indicating that it is derived
346 from red-lineage algae. In particular, since the Lhcx/Lhcsr clade showed monophyly with the CgLhcr9

347 homolog and Lhcf subfamily, it was demonstrated that the Lhcx subfamily is one of the new LHC
348 subfamily groups that arose in heterokont algae along with Lhcq, CgLhcr9 homolog, and Lhcf
349 subfamilies. Furthermore, since Lhcsr is conserved in both core green algae and streptophyte algae,
350 this supports the hypothesis proposed in Dittami et al. that the ancestor of extant green plants acquired
351 the Lhcx/Lhcsr subfamily through horizontal gene transfer from a red-lineage alga, presumably a
352 heterokont alga or haptophyte, before the last common ancestor of extant green plants. The estimated
353 divergence time of extant green plants into Streptophyta and Chlorophyta overlaps with the emergence
354 of heterokonts (Strassert et al., 2021), indicating that gene transfer of Lhcx/Lhcsr from heterokonts to
355 ancestral green plants could have occurred prior to this divergence event. It is difficult to determine
356 whether this gene transfer was merely a horizontal gene transfer or involved the acquisition of a
357 temporary red-lineage plastid, such as a kleptoplast. Additionally, looking at Figure 1, the
358 monophyletic clade of the green algae Lhca and Lhcb subfamilies does not form a monophyletic group
359 with the red algae Lhcr subfamily, and between them exist cryptophyte Lhcr and diatom Lhcr. This
360 does not negate the possibility that not only Lhcsr but also the Lhca and Lhcb subfamilies were
361 acquired through horizontal gene transfer. This result calls for reconsideration of the formation and
362 establishment of early chloroplasts.

363 Within Lhcx, Lhcx6_1, which exists at the most basal position, is present in *T. pseudonana* and
364 *Cyclotella cryptica* but not in *C. gracilis* or *Phaeodactylum tricornutum* (Figure 1, inset). This
365 Lhcx6_1 not only has an evolutionary distance from other typical Lhcx in the molecular phylogenetic
366 tree but also does not show a low NPQ phenotype when deficient (Nakayasu et al., 2024). Furthermore,
367 Lhcx6_1 directly binds to PSII and has a completely different assembly from *C. gracilis* PSII–FCPII
368 (Feng et al., 2023; Zhao et al., 2023). Based on these observations, it is considered that Lhcx6_1 is an
369 atypical Lhcx and does not mediate NPQ, and we argue that its classification within the Lhcx
370 subfamily should also be reconsidered.

371

372 **Spectroscopic Characteristics of Lhcx Quenching**

373 In this study, we successfully obtained NPQ signals at 140 ps around 687 nm by measuring time-
374 resolved fluorescence comparing frozen whole cells immediately after dark adaptation and HL
375 irradiation, reflecting the *in vivo* state (Figure 6, Supplemental Figure 7). By using the *lhcx1* mutant
376 that shows a clear phenotype with almost no NPQ induction, and by optimizing the dark adaptation
377 and HL exposure time to 30 minutes, we were able to clearly distinguish signals attributable to Lhcx-
378 mediated NPQ.

379 Our results provided the first report measuring the time-resolved fluorescence of mutants with near-
380 complete NPQ deficiency, resulting in a clear signal of NPQ. Even though several similar attempts on
381 diatoms and *Nannochloropsis* have been made, they could not find a clear NPQ signal in this approach
382 in the previous studies. For example, similar analyses were performed for the diatoms *C. meneghinia*
383 and *P. tricornutum* (Miloslavina et al., 2009). A different approach was taken regarding DAS fitting
384 compared to this study, with strong assumptions placed on the fluorescence signals of PSII and PSI,
385 and quenching signals like those observed in this study were not obtained. More detailed observations
386 of quenching using time-resolved fluorescence have been attempted in the diatom *C. meneghiniana*,
387 but the ~200 ps signal around 685 nm observed in this study was not observed; instead, a ~600 ps
388 quenching signal at 695 nm was observed and attributed to PSII (Chukhutsina et al., 2014). However,
389 since they only used WT, they could not conclude the signal of ~600 ps as NPQ depending on Lhcx.
390 In a similar approach, also using only WT of *Nannochloropsis*, a 214 ps signal at 685 nm in
391 *Nannochloropsis gaditana* was attributed to LHCII quenching, but it was not clear whether this was a
392 quenching signal due to the presence of Lhcx (Chukhutsina et al., 2017). A similar approach using
393 *lhcx* mutants has been performed in *P. tricornutum* (Taddei et al., 2018). However, the *lhcx1*
394 knockdown mutant of *P. tricornutum* showed limited decrease in the abundance of Lhcx1 and NPQ.

395 LL-grown *lhcx1*-knockdown mutants showed a slight decrease in NPQ, and HL-grown *lhcx1*-
396 knockdown showed no difference in NPQ because of the expression of Lhcx3, which is an isoform of
397 the Lhcx subfamily in *P. tricornutum*. Therefore, the observation and discussion of NPQ signal in
398 time-resolved fluorescence was limited in contrast to this study using *lhcx1*-knockout mutants, which
399 show minimal expression of other Lhcx isoforms (Supplemental Figure 10). Note that Buck and co-
400 workers created *Lhcx1*-knockout mutants of *P. tricornutum*, which showed a clearer drop in NPQ in
401 contrast to knock-down mutants; however, they did not report time-resolved fluorescence (Buck et al.,
402 2019). Considering these things together, this study provided the first clear NPQ signal in time-
403 resolved fluorescence analysis using almost-complete knock-out of Lhcx in Heterokonts, including
404 diatoms.

405 The spectroscopic characteristics of NPQ in diatoms differ notably from those in green algae. In
406 green alga *Chlamydomonas reinhardtii stt7-9* state-transition-less mutants, NPQ signals were
407 observed at 150 ps in time-resolved fluorescence and ~100 ps in transient absorption at physiological
408 temperature, similar to our time constant, but the NPQ signal from fluorescence was detected at 682
409 nm and attributed to LHCII fluorescence (Tian et al., 2019; Zheng et al., 2024). This wavelength
410 difference (682 nm vs. 687 nm) likely reflects differences in measurement temperatures and distinct
411 pigment compositions between the two algal groups, rather than fundamental mechanistic differences.

412 Time-resolved fluorescence measurements in whole cells revealed longer excitation energy transfer
413 times compared to isolated complexes. While excitation energy transfer from FCPII to the PSII core
414 in isolated $C_2S_2M_2$ PSII–FCPII occurs up to a time constant of 210 ps (Nagao et al., 2022), our
415 measurements in dark-adapted whole cells showed a significantly longer time constant of 640 ps
416 (Figure 6, Supplemental Figure 7). This threefold increase suggests that PSII–FCPII complexes *in vivo*
417 possess larger antenna systems than the isolated $C_2S_2M_2$ form, indicating the presence of additional
418 FCPs connected to the excitation energy network. These peripheral antenna complexes, likely

419 including L-FCPII dimers, extend the effective antenna size and modify energy transfer kinetics.

420

421 **The mechanism of Lhcx1-mediated NPQ**

422 The localization of diatom Lhcx has been debated for many years. Except for Lhcx6_1 associated
423 with PSII core (Feng et al., 2023; Zhao et al., 2023), the localization of Lhcx has been detected in free
424 FCP or bulk FCP (Lepetit et al., 2010; Grouneva et al., 2011), except for reports that *P. tricornutum*
425 Lhcx1/Lhcx2 bind to PSI (Grouneva et al., 2011). Additionally, in SDS-PAGE following CN-PAGE,
426 *T. pseudonana* Lhcx1 was detected as a free monomer (Zhou et al., 2024). In the 2D-CN/SDS-PAGE
427 of the diatom *C. gracilis* by Zhou et al. (2024), Lhcx1 was not detected. In this study, we utilized
428 Amphipol A8-35, a surfactant that enhances the stability of membrane proteins, to enable the
429 separation of diatom $C_2S_2M_2$ PSII–FCPII, which had been previously challenging with CN-PAGE
430 methods (Figure 7A). Under this condition, the dimer (L-dimer) consisting of CgLhcf12/CgLhcf2
431 (FCP-B/C) showed a broad band in the first dimension (Figure 7B), and a similar band pattern was
432 observed in the immunoblot for CgLhcx1 (Figure 7C). These findings suggest that CgLhcx1 may
433 interact with the FCP L-dimer.

434 Assuming the interaction between L-FCPII dimers and Lhcx1, we propose that Lhcx1-mediated
435 NPQ operates through two possible mechanisms: either Lhcx1 directly functions as the quenching
436 center, or quenching occurs through the L-dimer via its interaction with Lhcx1. This mechanism can
437 be classified within the framework of Q1 and Q2 quenching, where Q1 occurs in detached antenna
438 complexes and Q2 occurs in minor LHCs bound to the PSII core (Holzwarth et al., 2009; Miloslavina
439 et al., 2009; Chukhutsina et al., 2014). Given that L-FCPII dimers bind loosely to S/M-FCPII, Lhcx1-
440 mediated quenching likely represents Q1-type quenching occurring in the peripheral light-harvesting
441 antenna, although it is unclear whether the L-FCPII dimer detaches from PSII-S/M-FCPII.

442 The 140 ps quenching time constant observed in HL-treated whole cells is notably faster than

443 previously reported values for isolated FCP complexes. Isolated FCP-A tetramers and FCP-B/C dimers
444 have been reported to show characteristic quenching with time constants of 270 ps and 200 ps,
445 respectively (Nagao et al., 2013). This acceleration in whole cells may result from two factors: first,
446 isolated FCP-B/C complexes lack Lhcx proteins, which appear crucial for efficient quenching; second,
447 isolated complexes lack the native membrane environment, including the ΔpH gradient and three-
448 dimensional protein organization necessary for optimal quenching function. These results highlight
449 the importance of studying NPQ mechanisms in intact cellular systems rather than relying solely on
450 isolated protein complexes.
451
452 **Compensatory mechanisms to the Lhcx1 Deficiency**
453 The *lhcx1* strain, which lacks the most highly expressed Lhcx1 in *C. gracilis* created using genome
454 editing, induced almost no NPQ and showed higher PSII effective quantum yield and oxygen-evolving
455 activity compared to the WT when acclimated to HL. Since NPQ mutants in land plants show
456 decreased PSII electron transport activity, i.e., decreased effective quantum yield, under HL
457 acclimation (Yang et al., 2022), it is unusual that *lhcx1*, an NPQ mutant in this study, shows a higher
458 PSII effective quantum yield. Since *lhcx1* has a smaller antenna size even when dark-adapted after HL
459 acclimation (Figure 6, Supplemental Figure 7), the decrease in excitation energy acquisition per PSII
460 core is thought to contribute to a higher PSII effective quantum yield. Additionally, since the PSII
461 effective quantum yield increased even under LL conditions with the addition of CO_2 (Supplemental
462 Figure 9), and transcriptomic analysis revealed that *lhcx1* specifically enhances carbon fixation and
463 central carbon metabolism pathways under both ambient air and CO_2 conditions (Figure 8B), it is
464 likely that the increase in carbon fixation capacity in the downstream electron transport chain also
465 contributed to the improvement of PSII effective quantum yield. The activation of downstream
466 electron sinks can be observed under HL conditions (Figure 2C).

467 HL acclimation in *lhcx1* was also suggested by the pigment analysis (Figure 3C–F). Chl content per
468 cell decreased in *lhcx1*, and while the amount of Fx per Chl did not change, the amounts of
469 xanthophylls Dtx and Ddx increased. The de-epoxidation state (DEPS) calculated from Dtx and Ddx
470 also increased in *lhcx1* under HL, indicating that acclimation responses under HL are enhanced from
471 the perspective of pigment composition as well. Generally, in WT diatoms, the amount of Dtx is very
472 well correlated with NPQ intensity (Lavaud and Lepetit, 2013). However, since *lhcx1* strains show
473 almost no induction of NPQ despite increased Dtx amounts, the correlation between Dtx amount and
474 NPQ requires the presence of Lhcx. Although it is not clarified whether the increased xanthophylls in
475 *lhcx1* are incorporated in LHC/FCP, they may function as antioxidants in thylakoid membranes and
476 contribute to photoprotection. The above multiple photoprotection mechanisms that became apparent
477 in the absence of Lhcx1 would contribute to the adaptation in variable marine environments.

Materials and Methods

Phylogenetic Analysis of LHCs Across Various Photosynthetic Eukaryotic Lineages

LHC sequences were collected from genomes and transcriptomes included in the Phycocosm and EukProt databases, in addition to our previous dataset (Kumazawa et al., 2022; Kumazawa and Ifuku, 2024), following the previous method (Kumazawa and Ifuku, 2024). The LHCs in the dataset were obtained from red algae, early-diverging streptophyte green algae (Leliaert et al., 2012): *Mesostigma viride* NIES-296 (Liang et al., 2020) and *Klebsormidium nitens* NIES-2285 (Hori et al., 2014), diatoms: *C. gracilis* , *Thalassiosira pseudonana*, *Cyclotella cryptica*, *Phaeodactylum tricornutum*, and cryptophytes: *Guillardia theta* CCMP2712 (Curtis et al., 2012) and Cryptophyceae sp. (*Baffinella* sp.) CCMP2293 (Dorrell et al., 2023). As reference sequences for Lhcsr, *Chlamydomonas reinhardtii* Lhcsr1 (UniProt: P93664) and Lhcsr3.1 (UniProt: P0DO19), which is identical to Lhcsr3.2 (UniProt: P0DO18), were added. Redundant sequences were removed from the LHC protein sequences using CD-HIT (Fu et al., 2012), and alignment was performed with mafft-einsi v7.525, followed by manual curation (Katoh and Standley, 2013). The curated dataset was realigned, and trimming was performed using ClipKit v2.3.0 in smart-gap mode to remove unaligned sites (Steenwyk et al., 2020). The phylogenetic tree was estimated using IQ-TREE v2.3.6 with the Q.pfam+I+R7 model selected by ModelFinder based on LG and Q.pfam models (Kalyaanamoorthy et al., 2017; Minh et al., 2020; Minh et al., 2021), and visualized with iTOL v6 (Letunic and Bork, 2024). Ultra-fast bootstrap approximation (UFBoot) and SH-aLRT support (%) tests were performed with 1000 replicates each (Guindon et al., 2010; Hoang et al., 2018). The aBayes support test was also conducted (Anisimova et al., 2011). The annotation of LHC subfamilies in the phylogenetic tree was based on our previous studies (Kumazawa et al., 2022; Kumazawa and Ifuku, 2024) and drawn on the tree using InkScape software.

502 **Cultivation**

503 The marine centric diatom *C. gracilis* (UTEX LB 2658) was used for all analyses. Pre-cultivation
504 was performed in IMK medium —4% (w/v) sea salt (SIGMA S9883, US) or artificial seawater made
505 with Daigo's Artificial Seawater SP (Nihon Pharmaceutical MS, Japan) supplemented with 1x Daigo's
506 IMK medium (Nihon Pharmaceutical MS, Japan) and 0.2 mmol L^{-1} Na_2SiO_3— at 20ºC under
507 fluorescent lights at approximately 30 µmol photons m^{-2} s^{-1} with continuous shaking at 100 rpm.
508 Seven–eight-day or three-day cultivation was performed in IMK medium at 25ºC under warm white
509 LEDs at 30 µmol photons m^{-2} s^{-1} (LL) or 300 µmol photons m^{-2} s^{-1} (HL), with continuous aeration
510 of air or 3% (v/v) CO_2.

511

512 **Preparation of Thylakoid Membranes from *C. gracilis* and Spinach**

513 Diatom WT cells cultured under HL at 25ºC, 300 µmol photons m^{-2} s^{-1} for three days were
514 centrifuged at 1,200×*g*, 20ºC for 5 minutes to collect the cells, then resuspended in artificial seawater,
515 washed, and centrifuged again. After removing the supernatant, the pellet was resuspended in 1 mL of
516 artificial seawater, transferred to a 1.5 mL microcentrifuge tube, and centrifuged at 21,500×*g*, 4ºC for
517 5 minutes to obtain a pellet. The pellet was resuspended in 1 mL of cell disruption buffer (20 mM
518 Tricine-KOH (pH 7.6), 0.4 mol L^{-1} sorbitol, 10 (w/v) % PEG-6000, 10 mM EDTA), mixed with 0.5
519 g of 0.1 mm diameter glass beads, and processed with a bead beater for 10 seconds. The sample was
520 then well-chilled on ice, and the disruption process was repeated a total of three times. The supernatant
521 was centrifuged at 21,500×*g*, 4ºC for 5 minutes to obtain a pellet. The pellet was resuspended in 1 mL
522 of washing buffer (20 mmol L^{-1} Tricine-KOH (pH 7.6), 0.4 mol L^{-1} Sorbitol, 5 mmol L^{-1} $MgCl_2$, 2.5
523 mmol L^{-1} EDTA) and centrifuged at 50×*g*, 4ºC for 5 minutes. The portion containing thylakoid
524 membranes was carefully collected, avoiding the upper and lower contaminants, and centrifuged at
525 21,500×*g*, 4ºC for 5 minutes to obtain a thylakoid membrane pellet. The pellet was resuspended in

526 solubilization buffer (50 m mol L^{-1} imidazole-HCl (pH 7.0 at 4°C), 20 (v/v) % glycerol), and a portion
527 was taken to measure the concentrations of Chl *a* and *c* (Jeffrey and Humphrey, 1975). The thylakoid
528 membrane of spinach (*Spinacia oleracea*) was isolated from market spinach based on previously
529 reported methods (Yamamoto et al., 2011) using the modified buffer (50 mmol L^{-1} tricine-NaOH (pH
530 7.8 at room temperature), 0.4 L^{-1} sucrose, 10 mmol L^{-1} NaCl, 5 mmol L^{-1} $MgCl_2$). The thylakoid
531 membranes were adjusted to 1 μg μL^{-1} of Chl *a*+*c* with solubilization buffer (50 mM imidazole-HCl
532 (pH 7.0 at 4°C), 20 (v/v) % glycerol).
533
534 **2D-CN/SDS-PAGE**
535 The 4–13% gradient gel used for CN-PAGE was prepared according to existing methods (Järvi et
536 al., 2011; Kameo et al., 2021), and the entire CN-PAGE procedure followed the modified CN-PAGE
537 method using Amphipol A8-35 (Kameo et al., 2021). However, 75 mmol L^{-1} imidazole-HCl (pH 7.0
538 at 4ºC) was used in the 3x gel buffer, and 40 (w/v) % acrylamide/bis solution (37.5:1) (019-25655,
539 Fujifilm Wako, Japan) was used for acrylamide. The anode buffer contained 25 mmol L^{-1} imidazole-
540 HCl (pH 7.0 at 4ºC), and the cathode buffer contained 50 mmol L^{-1} Tricine, 7.5 mmol L^{-1} imidazole.
541 The Chl concentrations in resuspended thylakoids were measured (Jeffrey and Humphrey, 1975), and
542 thylakoid membranes were adjusted to 1 μg μL^{-1} of Chl *a*+*c* and Chl *a*+*b* with solubilization buffer
543 (50 mmol L^{-1} imidazole-HCl (pH 7.0 at 4°C), 20 (v/v) % glycerol) and resuspended. An equal volume
544 of 2 (w/v) % dodecyl-α-D-maltoside (α-DM, Anatrace, OH, USA) was added for solubilization, placed
545 on ice for 2 minutes, then centrifuged at 21,500×*g* for 2 minutes to remove insoluble residues. The
546 supernatant was mixed with half the volume of 2 (w/v) % amphipol A8-35 (Anatrace, OH, USA), and
547 5 μg of Chl in 15 μL was applied to each well. Electrophoresis was performed using MyPowerII 300
548 power supply (AE-8135, ATTO, Japan) at 40 V, 1 mA for 660 minutes at 4ºC with two mini gels
549 simultaneously. After electrophoresis, the gels were scanned with the scanner ES2200 (EPSON, Japan).

550 The CN-PAGE gels were immersed in 50 (v/v) % glycerol on ice, cut into gel strips, and stored at −
551 80ºC in 50 (v/v) % glycerol until use.
552 Gel strips were solubilized by immersing them in solubilization buffer (1% SDS and 50 mM
553 dithiothreitol (DTT) for 30 minutes at room temperature, and then applied to gels with a stacking gel
554 (pH 6.8) and separation gel (14% acrylamide (37.5:1), 6 mol L^{-1} Urea, pH 8.6). The Laemmli system
555 was used for electrophoresis. When the dye had electrophoresed to the bottom of the marker well at
556 250 V, 100 mA, the process was temporarily stopped, and Precision Plus Protein Dual Color Standards
557 (#1610374, BioRad, CA, USA) were applied. Electrophoresis was then continued at 250 V for 90
558 minutes. After electrophoresis, gels not used for immunoblotting were fluorescently stained with
559 Oriole fluorescent gel stain (#1610496, BioRad, CA, USA) for 100 minutes, gently rinsed with
560 distilled water, and then fluorescence was detected using the ChemiDoc Touch Imaging System (Bio-
561 Rad).
562
563 **Construction of hCas9 Vector**
564 The hCas9 sequence was amplified from the hCas9 vector (Addgene, plasmid #41815) using the
565 InF-hCas9-fw1 primer (TTTATAAAGCGGATCATGGACAAGAAGTACTCCATTGG) and InF-
566 hCas9-rv1 primer (AACAGCTTGCATGCCTCACACCTTCCTCTTCTTCTTG). The PCR product
567 was cloned into the linearized pCgNRp vector digested with BamHI and PstI using In-Fusion reaction
568 according to the manufacturer's protocol. The obtained clone vector was named pCgNRphCas9.
569
570 **Construction of pCgNRpble-Lhcx1-RGR Vector**
571 A 20-mer genome editing target sequence containing the PAM (protospacer adjacent motif)
572 sequence (NGG) for gRNA in the CRISPR/Cas9 system, GTTGCTATGCTTGCCGTTAT**TGG** (bold
573 indicates the PAM sequence), was selected. A system that expresses complete gRNA in cells via a

574 mRNA-type Pol II promoter by connecting self-processing ribozymes (Gao and Zhao, 2014; Zhang et
575 al., 2017) was used. This method was adapted to the genome editing system of *C. gracilis*. The genome
576 editing vector containing gRNA was constructed using three primers: Lhcx1-RGR-F1;
577 GACGAAACGAGTAAGCTCGTC**GTTGCTATGCTTGCCGTTAT**GTTTTAGAGCTAGAAATA
578 GCAAG (bold indicates the 20-mer sequence for gRNA target recognition excluding the PAM
579 sequence), Lhcx1-RGR-F2;
580 GTCAGGATCC**AGCAAC**CTGATGAGTCCGTGAGGACGAAACGAGTAAGCTCGTC (BamHI
581 restriction enzyme site is underlined, and bold indicates the complementary sequence of the first six
582 bases of the 20-mer for gRNA target recognition including the PAM sequence), and PstI-RGR-Rv;
583 ATATCTGCAGGTCCCATTCGCCATGCCGAAGC (PstI restriction enzyme site is underlined). The
584 PstI-RGR-Rv primer is a universal primer in this protocol. The first fragment (199 bp) was amplified
585 by PCR from pRS316-RGR-GFP (Addgene, plasmid #51056) using the Lhcx1-RGR-F1 and PstI-
586 RGR-Rv primers. The second fragment (231 bp) was amplified by PCR from the first purified PCR
587 product using the Lhcx1-RGR-F2 and PstI-RGR-Rv primers. The purified second product was
588 digested with BamHI (NEB) and PstI (NEB), and ligated with the pCgNRpble vector linearized with
589 BamHI and PstI. The final product was named pCgNRp^{ble}-Lhcx1-RGR.
590

591 **Transformation**

592 The electroporation transformation procedure using the Super electroporator NEPA21 Type-II
593 (NEPAGENE, Japan) followed previous reports (Miyahara et al., 2013; Ifuku et al., 2015; Ifuku and
594 Yan, 2020). The initial transformation of the *hCas9* gene into *C. gracilis* was performed using the
595 pCgNRphCas9 vector linearized with DraIII and SapI. Colonies were selected on IMK plates
596 containing the antibiotic Nourseothricin at 400 μg mL^{-1} (clonNAT; Hans Knoell Institute, Jena,
597 Germany). The introduced *hCas9* gene was confirmed by PCR using the first set: InF-hCas9-fw1

598 primer and hCas9-2088-Rv primer: CCTTAAAGGTGAGAGAGTCATCATGGATC, and another set:
599 hCas9-1965n-Fw primer: ATGAAACAGCTCAAGAGGCGCCGA and InF-hCas9-rv1 primer. The
600 hCas9 strain (hC9 strain) used for further genome editing was selected from eight transformants
601 screened by PCR and immunoblotting using anti-Cas9 antibody (described later).

602 The linearized pCgNRpble-Lhcx1-RGR was introduced into the hC9 strain by electroporation. This
603 was essentially the same as the transformation of hCas9. Before introducing the RGR vector, the vector
604 was linearized with HindIII (NEB) and concentrated to 850–1000 ng μL^{-1} by ethanol precipitation.
605 The amount of linearized vector was 5 μg per electroporation. Colonies were selected on IMK plates
606 containing the antibiotic Zeocin at 100 μg mL^{-1} (InvivoGen #ant-an-1, US CA). Mutations were
607 confirmed by Sanger sequencing of the products amplified by PCR using Lhcx1_seq_FW primer:
608 AGAGACTGTAAGGATTCGGA and Lhcx1_seq_RV primer: GAAGGAAGATCCCTCTACCT.

609

610 **Immunoblotting**

611 Diatom cells were collected and solubilized in sample buffer containing 62.5 mmol L^{-1} Tris–HCl
612 (pH 6.8), 2.5% (w/v) SDS, 10% (w/v) glycerol, 2.5% (v/v) 2-mercaptoethanol, and a trace amount of
613 bromophenol blue (BPB). Solubilization was performed by incubating at 98ºC for 6 minutes, followed
614 by 30 minutes at room temperature, and then centrifugation. The protein concentration was adjusted
615 to 30 μg/20 μL. Thirty micrograms of protein was applied to each lane of an 8% acrylamide separation
616 gel with a 3% acrylamide stacking gel and separated by SDS-PAGE. Proteins were transferred to an
617 Immobilon-P PVDF membrane (Millipore, MA, USA) and incubated with anti-Cas9 polyclonal
618 antibody (632607, Takara, Japan) at a 1:2000 dilution.

619 For the detection of Lhcx1, SDS-PAGE gels were prepared with a 15% acrylamide separation gel
620 and a 4.5% acrylamide stacking gel. Two μg of protein was applied to each lane and separated by SDS-
621 PAGE. The anti-Lhcx1 peptide antibody was produced against the synthetic peptide

"KEEYAPGDLRFDPFGLMP". After electrophoresis, the gel was desalted and equilibrated in Electron transfer buffer (25 mmol L^{-1} Tris, 192 mmol L^{-1} glycine, 20 (v/v) % methanol, 0.05 (w/v) % SDS). Subsequently, proteins were transferred from the gel to an Immobilon-P PVDF membrane (Millipore, Billerica, MA, USA) and incubated with anti-Lhcx1 antibody at a 1:5000 dilution. Immunoreactive proteins were detected using the Amersham ECL Prime Western Blotting Detection Reagent (Cytiva RPN2236) with the ChemiDoc Touch Imaging System (Bio-Rad).

PAM Fluorescence Measurement

Chl fluorescence by pulse-amplitude modulation was detected using an actinic light of 450 or 455 nm (blue) at 300 μmol photons m^{-2} s^{-1} with the NPQ2 protocol (200 seconds of light period and 390 seconds of dark recovery, with the first saturating pulse light in the light period at 10 seconds after the start of illumination) of AquaPen AP-100 or AP-110 (PSI, Czech Republic) using a bandpass filter (667 to 750 nm). The measuring pulse was set to 10%, and the super pulse (saturating pulse light) was set to 30% (equivalent to 900 μmol photons m^{-2} s^{-1}). Cells used in the NPQ2 protocol were dark-adapted for more than 10 minutes before measurement.

Oxygen-Evolving Activity Measurements

The diatom cells grown under HL conditions (200 μmol photons m^{-2} s^{-1} with rotational shaking at ~22ºC) were adjusted to a concentration of 5 μg Chl *a* mL^{-1} (Jeffrey and Humphrey, 1975), following the methods described in Nakayasu et al. (Nakayasu et al., 2024). Using a Clark-type oxygen electrode (Hansatech, UK) at 25°C, oxygen evolution was measured in the medium supplemented with 10 mM $NaHCO_3$. Cells were illuminated with white light at 300 μmol photons m^{-2} s^{-1}, and the cell suspension in the reaction chamber was continuously stirred with a magnetic stirrer during measurements.

646

647 **HPLC Pigment Analysis**

648 Cells cultured for 7–8 days under LL or HL conditions were collected by centrifugation at 1,500 x
649 *g* for 5 minutes, and the supernatant was removed. The pellet was immediately frozen in liquid nitrogen
650 and stored at −80 ºC until extraction. The frozen pellet was extracted using 100% acetone (Wako,
651 Japan) with sonication for 6 minutes in an ice-water bath. Subsequently, the sample was centrifuged
652 at 15,000 rpm for 5 minutes at 4 ºC. The resulting supernatant was filtered through a 0.45 nm
653 hydrophilic PTFE filter (SLPT0445NL, Hawach Scientific, IL, USA) and subjected to HPLC. The
654 HPLC method is based on Nagao, Ueno, et al. (2020) with modifications derived from Manuel Zapata
655 et al. (2000). The 0.25 mol L^{-1} pyridine contained in solution A was adjusted to pH 5.0 using acetic
656 acid. A Shimadzu HPLC system equipped with LC-20AD pumps and an SPD-M20A detector was
657 used for pigment composition analysis. The system was equipped with an Inertsil C8 reverse-phase
658 column (5020-01228, GL Sciences, Japan). The sample injection volume was 20 µL for each analysis.
659 Standard pigments of Chl *a*, fucoxanthin, diadinoxanthin, and diatoxanthin were purchased from DHI
660 (Denmark), analyzed similarly, and used to create calibration curves.

661

662 **77K Steady-State Fluorescence Spectra**

663 Cells for measurement were cultured under HL at 300 µmol photons m^{-2} s^{-1} at 25ºC for 3 days.
664 Samples were diluted with IMK medium and adjusted to 10 µg Chl *a*+*c*/150 µL. Chl concentration
665 was measured after extraction with 90% acetone (Jeffrey and Humphrey, 1975). The diluted samples
666 were treated in the dark or under HL at 300 µmol photons m^{-2} s^{-1} for 30 minutes and immediately
667 frozen in liquid nitrogen. Low-temperature steady-state fluorescence emission spectra of whole cells
668 were measured at 77K with excitation at 459 nm using a JASCO FP-8500 equipped with a PMU-130
669 liquid nitrogen cooling unit. The spectra were integrated from 5 consecutive measurements with a 2.5

nm sampling pitch. The spectra were normalized at the PSII CP47 peak (693–695 nm) (Andrizhiyevskaya et al., 2005; Nagao et al., 2010).

Time-Resolved Fluorescence and Fluorescence Decay-Associated Spectra

Samples were prepared for time-resolved fluorescence (TRF) spectral measurements using the same method as for steady-state measurements. TRF spectra were measured using a time-correlated single-photon counting system in the range of 670 nm to 750 nm with wavelength intervals of 1 nm and time intervals of 18.3 ps (Hamada et al., 2017). A picosecond pulsed diode laser (PiL047X; Advanced Laser Diode Systems) operating at 459 nm with a repetition frequency of 3 MHz was used as the excitation light source to excite Chl *c* and fucoxanthin, which are the main light-harvesting pigments in diatoms. Detailed conditions for TRF measurements were described in Nagao et al. (2020). Fluorescence decay-associated spectrum (spectra) (FDAS) was constructed by global analysis (Ye et al., 2025). The analysis of fluorescence decay $I_F(\lambda, t)$ at wavelength λ with the instrument response function $I_{IRF}(t)$ followed the function:

$$\boldsymbol{I_F(\lambda, t) = C \sum_{i=1}^{6} A_i(\lambda) \int_{-\infty}^{t} I_{IRF}(t')\, exp\left(-\frac{t-t'}{\tau_i}\right) dt'}$$

The time constants were set to $\tau_{1–6}$ = 40 ps, 140 ps, 640 ps, 1.6 ns, 3.8 ns, and 26 ns based on the analysis results of WT cells cultured under white LED light. $A_i(\lambda)$ represents each FDAS. The rise and decay components of fluorescence are indicated by negative and positive peaks, respectively. Positive and negative amplitudes in the same FDAS reflect energy transfer from pigments with positive amplitude to pigments with negative amplitude (Yokono et al., 2008; Akimoto et al., 2012). Positive amplitude without accompanying negative amplitude signifies energy quenching. For Figure 6 and Supplemental Figure 7, FDAS of each sample was normalized as,

$$\frac{A_i(\lambda)}{\int \sum_{i=1}^{6} A_i(\lambda)\, d\lambda} \times 100.$$

693 For easy viewing, a magnification factor 100 was used.

694

695 **Measurement of PSII Antenna Size**

696 Chl fluorescence induction curves of wild-type (WT) and three *lhcx1* mutants (*lhcx1-7*, *lhcx1-15*,
697 *lhcx1-234*) cultured under HL at 300 μmol photons m^{-2} s^{-1} at 25ºC for 3 days were measured using
698 a Fluorometer FL 3500 (PSI, Czech Republic) in the presence of 40 μM DCMU after 10 minutes of
699 dark adaptation (Nedbal et al., 1999). The cultures were grown in two independent batches. In the
700 measurement, Flash intensity was set to 50%, and Flash duration was set to 100 μs. The relative
701 antenna size was determined by measuring the initial slope of fluorescence rise during the first 1 μs
702 relative to the maximum fluorescence intensity. Four replicate measurements were performed for each
703 strain.

704 For data analysis, R statistical software (R version 4.4.0 (2024-04-24)) was used, utilizing the
705 tidyverse, readr, lme4, emmeans, and ggplot2 packages. To account for batch-specific variations,
706 antenna size values were normalized by the WT mean value within each batch. A linear mixed model
707 (LMM) was applied to the normalized data. Estimated marginal means were calculated, and multiple
708 comparisons were performed using the Tukey method. The threshold for statistical significance was
709 set at adjusted $p < 0.05$.

710

711 **RNA sequencing**

712 Cells were harvested during the exponential growth phase after three days of treatment exposure to
713 LL/HL and ambient/3%-CO_2-supplemented air aeration, frozen with liquid nitrogen and stored at −
714 80ºC until use. The frozen cells were crushed by bead-beating with 3-mm diameter zirconia beads.
715 Total RNA was extracted using the RNeasy Plant Mini Kit (Qiagen) following the Robertson
716 laboratory's protocol (https://wordpress.clarku.edu/debrobertson/laboratory-protocols/rna-extraction-

717 from-diatoms-using-the-rneasy-kit/). RNA-seq libraries were constructed using the NEBNext Ultra II
718 RNA Library Prep Kit for Illumina (Cat No. 7770) according to the manufacturer's instructions.
719 Paired-end sequencing (2 × 150 bp) was performed on an Illumina NovaSeq 6000 platform. Adapter
720 sequences (Read 1: AGATCGGAAGAGCACACGTCTGAACTCCAGTCA, Read 2:
721 AGATCGGAAGAGCGTCGTGTAGGGAAAGAGTGT) were trimmed from raw sequencing reads.
722 Prior to mapping, the gene structure annotation provided in ChaetoBase v1.1 (predicted_all.gff3) was
723 modified using the following procedures: (1) replacement of geneID attributes with Parent attributes
724 for transcripts lacking gene correspondence, (2) correction of transcripts incorrectly defined as genes,
725 and (3) addition of missing gene definitions using AGAT v1.0.0.

726 Clean reads were aligned to the *C. gracilis* reference genome (ChaetoBase v1.1) using STAR
727 v2.7.11b with the following parameters: --alignIntronMax 10000. Gene expression levels were
728 quantified using RSEM v1.3.3 with --strandedness reverse to account for Illumina stranded RNA-seq
729 protocol, and expected count matrices were generated for downstream analysis.

730

731 **Differential Gene Expression Analysis**

732 Statistical analysis of gene expression was performed using the edgeR package (v4.6.2) in R
733 (v4.5.0). Genes with low expression levels were filtered out by retaining only those with CPM (counts
734 per million) values exceeding the 20th percentile in at least one condition. A DGEList object was
735 created, and normalization factors were calculated using the TMM (trimmed mean of M-values)
736 method. Dispersion parameters were estimated using the estimateDisp function, and generalized linear
737 models (GLM) were fitted using glmQLFit.

738

739 **Statistical Contrasts and Hypothesis Testing**

740 To address the research objectives, the following statistical contrasts were performed:

741 1) Primary Analysis: HL Response Comparison

742 WT HL response: Air.HL.WT vs Air.LL.WT

743 lhcx1 HL response: Air.HL.lhcx1 vs Air.LL.lhcx1

744 Enhanced HL response in lhcx1: (Air.HL.lhcx1 - Air.LL.lhcx1) - (Air.HL.WT - Air.LL.WT)

745 2) Secondary Analysis: CO_2 Effect Validation

746 WT HL response under CO_2: CO_2.HL.WT vs CO_2.LL.WT

747 lhcx1 HL response under CO_2: CO_2.HL.lhcx1 vs CO_2.LL.lhcx1

748 Enhanced HL response in *lhcx1* under CO2: (CO2.HL.lhcx1 - CO_2.LL.lhcx1) -

749 (CO_2.HL.WT - CO_2.LL.WT)

750 Differential expression was determined using quasi-likelihood F-tests implemented in glmQLFTest.

751 P-values were adjusted for multiple testing using the Benjamini-Hochberg method, with an FDR

752 threshold of 0.05.

753

754 **Functional Enrichment Analysis**

755 KEGG pathway enrichment analysis was conducted using the enrichKEGG function from the

756 clusterProfiler package (v4.16.0). KEGG Orthology (KO) annotations for *C. gracilis* genes were

757 obtained from BLASTP searches against the KEGG database using BLASTKOALA. Only pathways

758 with q-value < 0.05 were considered significantly enriched.

Acknowledgment

This work was supported in part by JSPS KAKENHI grant nos. JP22KJ2017 (M.K.), JP24H02086 (S.A.), JP23KJ1361 (Ko.I.), JP23H02347 (Ke.I. and S.A.), JP24H02081 (Ke.I.), and a grant from the Institute for Fermentation, Osaka, Japan (Ke.I.). We would like to thank Ms. Dongyi Yan for her help in the establishment of knock-out mutants.

Competing Interests

Authors HH, AS, and SI are employed by the NTT, Inc.

Data Availability

RNA-seq data in this study were deposited with link to BioProject accession number PRJDB12222 in the NCBI BioProject database, and the list of the data in Supplemental Data 1.

Author Contributions

M.K. and Ke.I. conceived the project; M.K. performed phylogenetic analysis, 2D-CN/SDS-PAGE, growth experiments, PAM analyses, absorbance spectrum analyses, 77K emission fluorescence analysis, antenna size measurements, and RNA-seq *in silico* analysis, and prepared samples for ime-resolved fluorescence analyses; S.A. performed time-resolved fluorescence analyses; A.T. conceived the methodology of 2D-CN/SDS-PAGE; Ko.I. measured and analyzed oxygen-evolving activity; S.T. measured pigments; H.H., A.S., and S.I. performed RNA-seq and provided funding; N.I. conceived methodology of SDS-PAGE and immunoblotting; N.I.-K. and Y.K. provided anti-Lhcx1 antibody. M.K. drafted the original manuscript, and Ke.I. revised and edited the final manuscript. All authors contributed to the discussion of the results and improvement of the manuscript.

References

Akimoto S, Yokono M, Hamada F, Teshigahara A, Aikawa S, Kondo A (2012) Adaptation of light-harvesting systems of Arthrospira platensis to light conditions, probed by time-resolved fluorescence spectroscopy. Biochim. Biophys. Acta Bioenerg. pp 1483–1489

Allorent G, Lefebvre-Legendre L, Chappuis R, Kuntz M, Truong TB, Niyogi KK, Ulm R, Goldschmidt-Clermont M (2016) UV-B photoreceptor-mediated protection of the photosynthetic machinery in Chlamydomonas reinhardtii. Proc Natl Acad Sci U S A **113**: 14864–14869

Allorent G, Tokutsu R, Roach T, Peers G, Cardol P, Girard-Bascou J, Seigneurin-Berny D, Petroutsos D, Kuntz M, Breyton C, et al (2013) A Dual Strategy to Cope with High Light in *Chlamydomonas reinhardtii* . Plant Cell **25**: 545–557

Andrizhiyevskaya EG, Chojnicka A, Bautista JA, Diner BA, Van Grondelle R, Dekker JP (2005) Origin of the F685 and F695 fluorescence in Photosystem II. Photosynth. Res. pp 173–180

Anisimova M, Gil M, Dufayard JF, Dessimoz C, Gascuel O (2011) Survey of branch support methods demonstrates accuracy, power, and robustness of fast likelihood-based approximation schemes. Syst Biol **60**: 685–699

Bailleul B, Rogato A, De Martino A, Coesel S, Cardol P, Bowler C, Falciatore A, Finazzi G (2010) An atypical member of the light-harvesting complex stress-related protein family modulates diatom responses to light. Proc Natl Acad Sci U S A **107**: 18214–18219

Buck JM, Kroth PG, Lepetit B (2021) Identification of sequence motifs in Lhcx proteins that confer qE-based photoprotection in the diatom Phaeodactylum tricornutum. Plant Journal **108**: 1721–1734

Buck JM, Sherman J, Bártulos CR, Serif M, Halder M, Henkel J, Falciatore A, Lavaud

806 **J, Gorbunov MY, Kroth PG, et al** (2019) Lhcx proteins provide photoprotection via thermal
807 dissipation of absorbed light in the diatom Phaeodactylum tricornutum. Nat Commun. doi:
808 10.1038/s41467-019-12043-6

809 **Chukhutsina VU, Büchel C, Van Amerongen H** (2014) Disentangling two non-
810 photochemical quenching processes in Cyclotella meneghiniana by spectrally-resolved
811 picosecond fluorescence at 77 K. Biochim Biophys Acta Bioenerg **1837**: 899–907

812 **Chukhutsina VU, Fristedt R, Morosinotto T, Croce R** (2017) Photoprotection strategies of
813 the alga Nannochloropsis gaditana. Biochim Biophys Acta Bioenerg **1858**: 544–552

814 **Croteau D, Jaubert M, Falciatore A, Bailleul B** (2025) Pennate diatoms make non-
815 photochemical quenching as simple as possible but not simpler. Nature Communications . doi:
816 10.1038/s41467-025-57298-4

817 **Curtis BA, Tanifuji G, Maruyama S, Gile GH, Hopkins JF, Eveleigh RJM, Nakayama T,**
818 **Malik SB, Onodera NT, Slamovits CH, et al** (2012) Algal genomes reveal evolutionary
819 mosaicism and the fate of nucleomorphs. Nature **492**: 59–65

820 **Dittami SM, Michel G, Collén J, Boyen C, Tonon T** (2010) Chlorophyll-binding proteins
821 revisited - a multigenic family of light-harvesting and stress proteins from a brown algal
822 perspective. BMC Evol Biol **10**: 365

823 **Dorrell RG, Kuo A, Füssy Z, Richardson EH, Salamov A, Zarevski N, Freyria NJ,**
824 **Ibarbalz FM, Jenkins J, Karlusich JJP, et al** (2023) Convergent evolution and horizontal gene
825 transfer in Arctic Ocean microalgae. Life Sci Alliance. doi: 10.26508/lsa.202201833

826 **Feng Y, Li Z, Li X, Shen L, Liu X, Zhou C, Zhang J, Sang M, Han G, Yang W, et al** (2023)
827 Structure of a diatom photosystem II supercomplex containing a member of Lhcx family and
828 dimeric FCPII. Sci Adv. doi: 10.1126/sciadv.adi8446

829 **Fu L, Niu B, Zhu Z, Wu S, Li W** (2012) CD-HIT: Accelerated for clustering the next-

generation sequencing data. Bioinformatics **28**: 3150–3152

Gao Y, Zhao Y (2014) Self-processing of ribozyme-flanked RNAs into guide RNAs in vitro and in vivo for CRISPR-mediated genome editing. J Integr Plant Biol **56**: 343–349

Giossi CE, Wünsch MA, Dautermann O, Schober AF, Buck JM, Kroth PG, Lohr M, Lepetit B (2025) Both major xanthophyll cycles present in nature promote non-photochemical quenching in a model diatom. Plant Physiol kiaf371

Giovagnetti V, Jaubert M, Shukla MK, Ungerer P, Bouly JP, Falciatore A, Ruban A V. (2022) Biochemical and molecular properties of LHCX1, the essential regulator of dynamic photoprotection in diatoms. Plant Physiol **188**: 509–525

Goss R, Lepetit B (2015) Biodiversity of NPQ. J Plant Physiol **172**: 13–32

Grouneva I, Rokka A, Aro EM (2011) The thylakoid membrane proteome of two marine diatoms outlines both diatom-specific and species-specific features of the photosynthetic machinery. J Proteome Res **10**: 5338–5353

Guindon S, Dufayard JF, Lefort V, Anisimova M, Hordijk W, Gascuel O (2010) New algorithms and methods to estimate maximum-likelihood phylogenies: Assessing the performance of PhyML 3.0. Syst Biol **59**: 307–321

Hamada F, Murakami A, Akimoto S (2017) Adaptation of Divinyl Chlorophyll a/b-Containing Cyanobacterium to Different Light Conditions: Three Strains of Prochlorococcus marinus. Journal of Physical Chemistry B **121**: 9081–9090

Hoang DT, Chernomor O, von Haeseler A, Minh BQ, Vinh LS (2018) UFBoot2: Improving the Ultrafast Bootstrap Approximation. Molecular biology and evolution. Mol Biol Evol **35**: 518–522

Holzwarth AR, Miloslavina Y, Nilkens M, Jahns P (2009) Identification of two quenching sites active in the regulation of photosynthetic light-harvesting studied by time-resolved

fluorescence. Chem Phys Lett **483**: 262–267

Hori K, Maruyama F, Fujisawa T, Togashi T, Yamamoto N, Seo M, Sato S, Yamada T, Mori H, Tajima N, et al (2014) Klebsormidium flaccidum genome reveals primary factors for plant terrestrial adaptation. Nat Commun. doi: 10.1038/ncomms4978

Huang W, Daboussi F (2017) Genetic and metabolic engineering in diatoms. Philosophical Transactions of the Royal Society B: Biological Sciences. doi: 10.1098/rstb.2016.0411

Ifuku K, Yan D (2020) Efficient Transformation of the Diatoms Phaeodactylum tricornutum by Multipulse Electroporation. Methods in Molecular Biology. doi: 10.1007/978-1-4939-9740-4_18

Ifuku K, Yan D, Miyahara M, Inoue-Kashino N, Yamamoto YY, Kashino Y (2015) A stable and efficient nuclear transformation system for the diatom Chaetoceros gracilis. Photosynth Res **123**: 203–211

Im SH, Lepetit B, Mosesso N, Shrestha S, Weiss L, Nymark M, Roellig R, Wilhelm C, Isono E, Kroth PG (2024) Identification of promoter targets by Aureochrome 1a in the diatom Phaeodactylum tricornutum. J Exp Bot **75**: 1834–1851

Ishihara T, Ifuku K, Yamashita E, Fukunaga Y, Nishino Y, Miyazawa A, Kashino Y, Inoue-Kashino N (2015) Utilization of light by fucoxanthin–chlorophyll-binding protein in a marine centric diatom, Chaetoceros gracilis. Photosynth Res **126**: 437–447

Järvi S, Suorsa M, Paakkarinen V, Aro EM (2011) Optimized native gel systems for separation of thylakoid protein complexes: Novel super- and mega-complexes. Biochemical Journal **439**: 207–214

Jeffrey SW, Humphrey GF (1975) New spectrophotometric equations for determining chlorophylls a, b, c1 and c2 in higher plants, algae and natural phytoplankton. Biochemie und Physiologie der Pflanzen **167**: 191–194

878 **Kalyaanamoorthy S, Minh BQ, Wong TKF, von Haeseler A, Jermiin LS** (2017)
879 ModelFinder: fast model selection for accurate phylogenetic estimates. Nat Methods **14**: 587–
880 589

881 **Kameo S, Aso M, Furukawa R, Matsumae R, Yokono M, Fujita T, Tanaka A, Tanaka R,**
882 **Takabayashi A** (2021) Substitution of Deoxycholate with the Amphiphilic Polymer Amphipol
883 A8-35 Improves the Stability of Large Protein Complexes during Native Electrophoresis. Plant
884 Cell Physiol **62**: 348–355

885 **Katoh K, Standley DM** (2013) MAFFT Multiple Sequence Alignment Software Version 7:
886 Improvements in Performance and Usability. Mol Biol Evol **30**: 772–780

887 **Koziol AG, Borza T, Ishida KI, Keeling P, Lee RW, Durnford DG** (2007) Tracing the
888 evolution of the light-harvesting antennae in chlorophyll a/b-containing organisms. Plant Physiol
889 **143**: 1802–1816

890 **Kumazawa M, Ifuku K** (2024) Unraveling the evolutionary trajectory of LHCI in red-lineage
891 algae: Conservation, diversification, and neolocalization. iScience **27**: 110897

892 **Kumazawa M, Nishide H, Nagao R, Inoue-Kashino N, Shen J, Nakano T, Uchiyama I,**
893 **Kashino Y, Ifuku K** (2022) Molecular phylogeny of fucoxanthin-chlorophyll *a* / *c* proteins from
894 *Chaetoceros gracilis* and Lhcq/Lhcf diversity. Physiol Plant **174**: e13598

895 **Lavaud J, Kroth PG** (2006) In diatoms, the transthylakoid proton gradient regulates the
896 photoprotective non-photochemical fluorescence quenching beyond its control on the
897 xanthophyll cycle. Plant Cell Physiol **47**: 1010–1016

898 **Lavaud J, Lepetit B** (2013) An explanation for the inter-species variability of the
899 photoprotective non-photochemical chlorophyll fluorescence quenching in diatoms. Biochim
900 Biophys Acta Bioenerg **1827**: 294–302

901 **Leliaert F, Smith DR, Moreau H, Herron MD, Verbruggen H, Delwiche CF, De Clerck**

O (2012) Phylogeny and Molecular Evolution of the Green Algae. CRC Crit Rev Plant Sci **31**: 1–46

Lepetit B, Volke D, Gilbert M, Wilhelm C, Goss R (2010) Evidence for the existence of one antenna-associated, lipid-dissolved and two protein-bound pools of diadinoxanthin cycle pigments in diatoms. Plant Physiol **154**: 1905–1920

Letunic I, Bork P (2024) Interactive Tree of Life (iTOL) v6: Recent updates to the phylogenetic tree display and annotation tool. Nucleic Acids Res **52**: W78–W82

Li X-P, Bjo O, Rkman[2] È, Shih[2] C, Grossman[2] AR, Rosenquist[3] M, Jansson[3] S, Niyogi KK (2000) A pigment-binding protein essential for regulation of photosynthetic light harvesting.

Lohr M, Wilhelm C (1999) Algae displaying the diadinoxanthin cycle also possess the violaxanthin cycle.

Malnoë A (2018) Photoinhibition or photoprotection of photosynthesis? Update on the (newly termed) sustained quenching component qH. Environ Exp Bot **154**: 123–133

Manuel Zapata, Francisco Rodríguez, José L. Garrido (2000) Separation of chlorophylls and carotenoids from marine phytoplankton: a new HPLC method using a reversed phase C8 column and pyridine-containing mobile phases. Mar Ecol Prog Ser **195**: 29–45

Miloslavina Y, Grouneva I, Lambrev PH, Lepetit B, Goss R, Wilhelm C, Holzwarth AR (2009) Ultrafast fluorescence study on the location and mechanism of non-photochemical quenching in diatoms. Biochim Biophys Acta Bioenerg **1787**: 1189–1197

Minagawa J, Tokutsu R (2015) Dynamic regulation of photosynthesis in *Chlamydomonas reinhardtii*. The Plant Journal **82**: 413–428

Minh BQ, Dang CC, Vinh LS, Lanfear R (2021) QMaker: Fast and Accurate Method to Estimate Empirical Models of Protein Evolution. Syst Biol **70**: 1046–1060

Minh BQ, Schmidt HA, Chernomor O, Schrempf D, Woodhams MD, von Haeseler A,

Lanfear R (2020) IQ-TREE 2: New Models and Efficient Methods for Phylogenetic Inference in the Genomic Era. Mol Biol Evol **37**: 1530–1534

Miyahara M, Aoi M, Inoue-Kashino N, Kashino Y, Ifuku K (2013) Highly efficient transformation of the diatom phaeodactylum tricornutum by multi-pulse electroporation. Biosci Biotechnol Biochem **77**: 874–876

Nagao R, Ishii A, Tada O, Suzuki T, Dohmae N, Okumura A, Iwai M, Takahashi T, Kashino Y, Enami I (2007) Isolation and characterization of oxygen-evolving thylakoid membranes and Photosystem II particles from a marine diatom Chaetoceros gracilis. Biochim Biophys Acta Bioenerg **1767**: 1353–1362

Nagao R, Kato K, Ifuku K, Suzuki T, Kumazawa M, Uchiyama I, Kashino Y, Dohmae N, Akimoto S, Shen J-R, et al (2020a) Structural basis for assembly and function of a diatom photosystem I-light-harvesting supercomplex. Nat Commun **11**: 2481

Nagao R, Kato K, Kumazawa M, Ifuku K, Yokono M, Suzuki T, Dohmae N, Akita F, Akimoto S, Miyazaki N, et al (2022) Structural basis for different types of hetero-tetrameric light-harvesting complexes in a diatom PSII-FCPII supercomplex. Nat Commun **13**: 1764

Nagao R, Kato K, Suzuki T, Ifuku K, Uchiyama I, Kashino Y, Dohmae N, Akimoto S, Shen J-R, Miyazaki N, et al (2019) Structural basis for energy harvesting and dissipation in a diatom PSII–FCPII supercomplex. Nat Plants **5**: 890–901

Nagao R, Tomo T, Noguchi E, Nakajima S, Suzuki T, Okumura A, Kashino Y, Mimuro M, Ikeuchi M, Enami I (2010) Purification and characterization of a stable oxygen-evolving Photosystem II complex from a marine centric diatom, Chaetoceros gracilis. Biochim Biophys Acta Bioenerg **1797**: 160–166

Nagao R, Tomo T, Noguchi E, Suzuki T, Okumura A, Narikawa R, Enami I, Ikeuchi M (2012) Proteases are associated with a minor fucoxanthin chlorophyll a/c-binding protein from

the diatom, Chaetoceros gracilis. Biochim Biophys Acta Bioenerg **1817**: 2110–2117

Nagao R, Ueno Y, Akimoto S, Shen JR (2020b) Effects of CO2 and temperature on photosynthetic performance in the diatom Chaetoceros gracilis. Photosynth Res **146**: 189–195

Nagao R, Yokono M, Akimoto S, Tomo T (2013) High excitation energy quenching in fucoxanthin chlorophyll a/c-binding protein complexes from the diatom Chaetoceros gracilis. Journal of Physical Chemistry B **117**: 6888–6895

Nagao R, Yokono M, Ueno Y, Shen JR, Akimoto S (2020c) Excitation-Energy Transfer and Quenching in Diatom PSI-FCPI upon P700 Cation Formation. Journal of Physical Chemistry B **124**: 1481–1486

Nakayasu M, Akimoto S, Yoneda K, Ikuta S, Shimakawa G, Matsuda Y (2024) Different functions of Lhcx isoforms in photoprotective mechanism in the marine diatom *Thalassiosira pseudonana*. BioRxiv. doi: 10.1101/2024.04.16.589823

Nedbal L, Trtflek M, Kaftan D (1999) Flash fluorescence induction: a novel method to study regulation of Photosystem II.

Niyogi KK (2004) Is PsbS the site of non-photochemical quenching in photosynthesis? J Exp Bot **56**: 375–382

Niyogi KK (2000) Safety valves for photosynthesis. Curr Opin Plant Biol **3**: 455–460

Niyogi KK, Grossman AR, Björkman O (1998) Arabidopsis Mutants Define a Central Role for the Xanthophyll Cycle in the Regulation of Photosynthetic Energy Conversion. Plant Cell **10**: 1121–1134

Park S, Steen CJ, Lyska D, Fischer AL, Endelman B, Iwai M, Niyogi KK, Fleming GR (2019) Chlorophyll–carotenoid excitation energy transfer and charge transfer in Nannochloropsis oceanica for the regulation of photosynthesis. Proc Natl Acad Sci U S A **116**: 3385–3390

Peers G, Truong TB, Ostendorf E, Busch A, Elrad D, Grossman AR, Hippler M, Niyogi KK (2009) An ancient light-harvesting protein is critical for the regulation of algal photosynthesis. Nature **462**: 518–521

Petroutsos D, Tokutsu R, Maruyama S, Flori S, Greiner A, Magneschi L, Cusant L, Kottke T, Mittag M, Hegemann P, et al (2016) A blue-light photoreceptor mediates the feedback regulation of photosynthesis. Nature **537**: 563–566

Pierella Karlusich JJ, Cosnier K, Zinger L, Henry N, Nef C, Bernard G, Scalco E, Dvorak E, Wincker P, Sunagawa S, et al (2025) Patterns and drivers of diatom diversity and abundance in the global ocean. Nature Communications . doi: 10.1038/s41467-025-58027-7

Pierella Karlusich JJ, Ibarbalz FM, Bowler C (2020) Phytoplankton in the *Tara* Ocean. Ann Rev Mar Sci **12**: 233–265

Steenwyk JL, Buida TJ, Li Y, Shen X-X, Rokas A (2020) ClipKIT: A multiple sequence alignment trimming software for accurate phylogenomic inference. PLoS Biol **18**: e3001007

Strassert JFH, Irisarri I, Williams TA, Burki F (2021) A molecular timescale for eukaryote evolution with implications for the origin of red algal-derived plastids. Nat Commun **12**: 1879

Taddei L, Chukhutsina VU, Lepetit B, Stella GR, Bassi R, van Amerongen H, Bouly JP, Jaubert M, Finazzi G, Falciatore A (2018) Dynamic changes between two LHCX-related energy quenching sites control diatom photoacclimation. Plant Physiol **177**: 953–965

Taparia Y, Dolui AK, Boussiba S, Khozin-Goldberg I (2022) Multiplexed Genome Editing via an RNA Polymerase II Promoter-Driven sgRNA Array in the Diatom Phaeodactylum tricornutum: Insights Into the Role of StLDP. Front Plant Sci. doi: 10.3389/fpls.2021.784780

Tian L, Nawrocki WJ, Liu X, Polukhina I, Van Stokkum IHM, Croce R (2019) PH dependence, kinetics and light-harvesting regulation of nonphotochemical quenching in Chlamydomonas. Proc Natl Acad Sci U S A **116**: 8320–8325

Tokutsu R, Fujimura-Kamada K, Matsuo T, Yamasaki T, Minagawa J (2019a) The CONSTANS flowering complex controls the protective response of photosynthesis in the green alga Chlamydomonas. Nat Commun. doi: 10.1038/s41467-019-11989-x

Tokutsu R, Fujimura-Kamada K, Yamasaki T, Matsuo T, Minagawa J (2019b) Isolation of photoprotective signal transduction mutants by systematic bioluminescence screening in Chlamydomonas reinhardtii. Sci Rep. doi: 10.1038/s41598-019-39785-z

Wang W, Yu L-J, Xu C, Tomizaki T, Zhao S, Umena Y, Chen X, Qin X, Xin Y, Suga M, et al (2019) Structural basis for blue-green light harvesting and energy dissipation in diatoms. Science (1979). doi: 10.1126/science.aav0365

Xu C, Pi X, Huang Y, Han G, Chen X, Qin X, Huang G, Zhao S, Yang Y, Kuang T, et al (2020) Structural basis for energy transfer in a huge diatom PSI-FCPI supercomplex. Nat Commun **11**: 5081

Yamamoto Y, Leng J, Shen J-R (2011) Isolation of Photosystem II-Enriched Membranes and the Oxygen-Evolving Complex Subunit Proteins from Higher Plants. *In* R Carpentier, ed, Photosynthesis Research Protocols. Humana Press, Totowa, NJ, pp 1–10

Yang YN, Le TTL, Hwang JH, Zulfugarov IS, Kim EH, Kim HU, Jeon JS, Lee DH, Lee CH (2022) High Light Acclimation Mechanisms Deficient in a PsbS-Knockout Arabidopsis Mutant. Int J Mol Sci. doi: 10.3390/ijms23052695

Ye Z, Sawada M, Iwasa M, Moriyama R, Dey D, Furutani M, Kitao M, Hara T, Tanaka A, Kishimoto J, et al (2025) Revisiting the early light-induced protein hypothesis in the sustained thermal dissipation mechanism in yew leaves. J Exp Bot **76**: 513–531

Yokono M, Akimoto S, Tanaka A (2008) Seasonal changes of excitation energy transfer and thylakoid stacking in the evergreen tree Taxus cuspidata: How does it divert excess energy from photosynthetic reaction center? Biochim Biophys Acta Bioenerg **1777**: 379–387

1022 **Zhang H, Xiong X, Guo K, Zheng M, Cao T, Yang Y, Song J, Cen J, Zhang J, Jiang Y, et**
1023 **al** (2024) A rapid aureochrome opto-switch enables diatom acclimation to dynamic light. Nat
1024 Commun **15**: 5578
1025 **Zhang T, Gao Y, Wang R, Zhao Y** (2017) Production of Guide RNAs in vitro and in vivo
1026 for CRISPR Using Ribozymes and RNA Polymerase II Promoters. Bio Protoc. doi:
1027 doi:10.21769/BioProtoc.2148
1028 **Zhao S, Shen L, Li X, Tao Q, Li Z, Xu C, Zhou C, Yang Y, Sang M, Han G, et al** (2023)
1029 Structural insights into photosystem II supercomplex and trimeric FCP antennae of a centric
1030 diatom Cyclotella meneghiniana. Nat Commun **14**: 8164
1031 **Zheng M, Pang X, Chen M, Tian L** (2024) Ultrafast energy quenching mechanism of
1032 LHCSR3-dependent photoprotection in Chlamydomonas. Nat Commun **15**: 4437
1033 **Zhou C, Feng Y, Li Z, Shen L, Li X, Wang Y, Han G, Kuang T, Liu C, Shen J-R, et al**
1034 (2024) Structural and spectroscopic insights into fucoxanthin chlorophyll a/c-binding proteins
1035 of diatoms in diverse oligomeric states. Plant Commun **5**: 101041
1036
1037

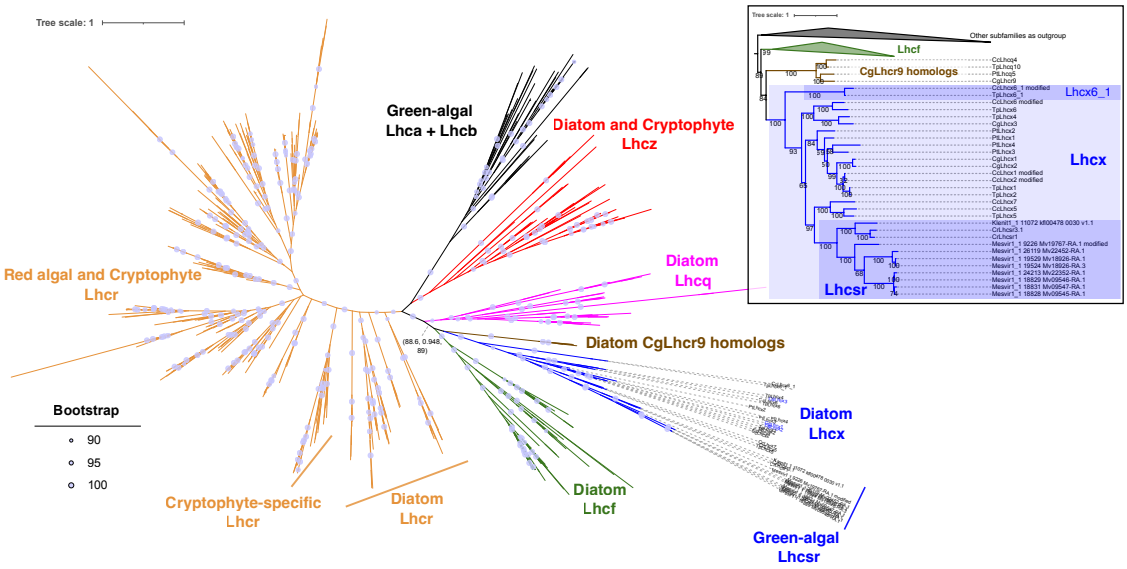

Figure 1. Molecular Phylogenetic Tree of Light-Harvesting Complexes (LHCs) from Red and Green Evolutionary Lineages

LHC sequences were obtained from red algae, green algae *Mesostigma viride* NIES-296 (Mesvir1_1) and *Klebsormidium nitens* NIES-2285 (Klepit1_1), diatoms: *Chaetoceros gracilis* (Cg), *Thalassiosira pseudonana* (Tp), *Cyclotella cryptica* (Cc), *Phaeodactylum tricornutum* (Pt), and cryptophytes: *Guillardia theta* CCMP2712 and Cryptophyceae sp. (*Baffinella* sp.) CCMP2293. These were combined with reference sequences for Lhcsr from *Chlamydomonas reinhardtii*: Lhcsr1 (UniProt: P93664) and Lhcsr3.1 (UniProt: P0DO19), which is identical to Lhcsr3.2 (UniProt: P0DO18), and a molecular phylogenetic tree was constructed using IQ-TREE2. The phylogenetic tree is displayed as an unrooted tree, and the inset tree is rerooted with the other LHC family members except for Lhcx, Lhcf, and CgLhcr9 homologs. LHC subfamilies, Lhcr, Lhcz, Lhcq, Lhcf, Lhcx, Lhca/Lhcb, and CgLhcr9 homologs, are indicated by orange, red, magenta, green, blue, black, and brown, respectively. Red algal and Cryptophyte Lhcrs are in the left part of the tree, Lhcrs expect for Cryptophyte-specific Lhcrs and Diatom Lhcrs. Detailed annotations are shown only for the Lhcx/Lhcsr subfamily. Circles on nodes indicate ultra-fast bootstrap support values of 90% or higher.

1054 Numbers in parentheses indicate SH-aLRT support values (%) / aBayes support values / ultra-fast

1055 bootstrap support values (%). Numbers in the inset tree are ultra-fast bootstrap support values (%).

1056

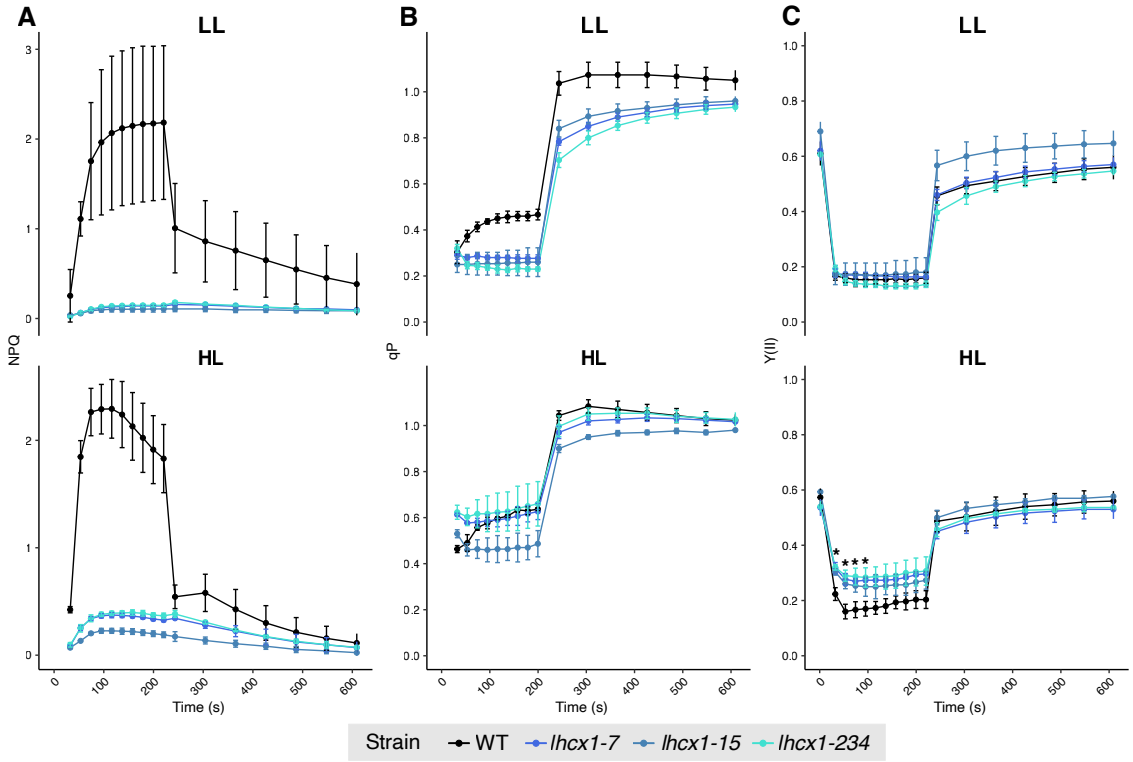

1057

1058 **Figure 2. PAM Fluorescence Measurements of *C. gracilis* Wild-Type and *lhcx1* Strains Cultured**

1059 **with Aeration for 7–8 Days Under Low Light (LL) and High Light (HL)**

1060 A) NPQ of LL and HL cultures. B) qP of LL and HL cultures. C) PSII effective quantum yield Y(II)

1061 of LL and HL cultures. * indicates that adjusted $p < 0.05$ by Tukey's HSD test was satisfied between

1062 the wild-type and all *lhcx1* strains. The points in each figure represent mean ± standard deviation with

1063 biological replicates of $n = 3$.

1064

1065

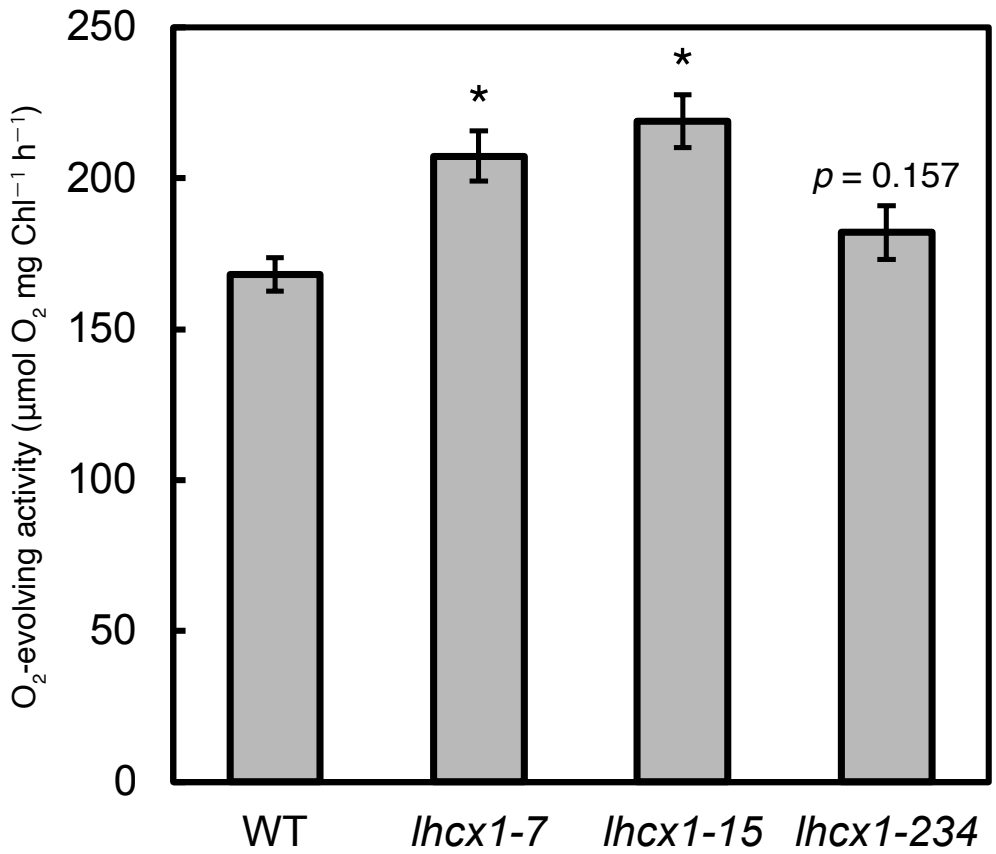

Figure 3. Oxygen-Evolving Activity of *C. gracilis* Wild-Type and *lhcx1* Strains

This figure shows the oxygen-evolving activity of *C. gracilis* wild-type (WT) and three *lhcx1* mutant strains (*lhcx1-7*, *lhcx1-15*, and *lhcx1-234*). Measurements were conducted under a light intensity of 300 μmol photons m^{-2} s^{-1} in the presence of 10 mM $NaHCO_3$. Data are presented as mean ± standard deviation ($n = 3$). Statistical analysis was performed using Dunnett's test to compare each mutant strain with the wild-type (WT). Asterisks (*) indicate $p<0.001$, while other actual p-values are shown in the graph.

1074

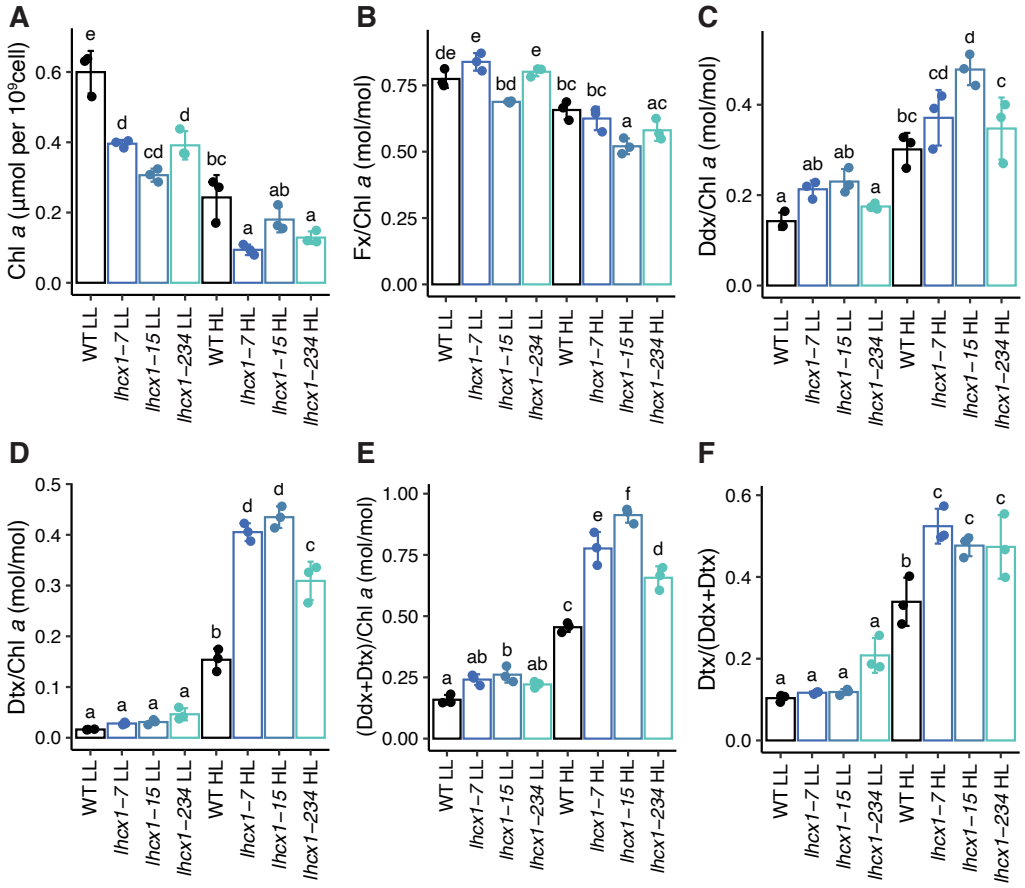

1075

1076 **Figure 4. Pigment Analysis of Low Light (LL) and High Light (HL) Cultures**

1077 A) Chlorophyll (Chl) *a* content per 10^9 cells. B) Fucoxanthin (Fx) content per Chl *a*. C)

1078 Diadinoxanthin (Ddx) content per Chl *a*. D) Diatoxanthin (Dtx) content per Chl *a*. E) Ddx+Dtx content

1079 per Chl *a*. F) De-epoxidation state (DEPS = [Dtx]/([Dtx]+[Ddx])). Data are presented as mean ±

1080 standard deviation (n = 3). Different alphabets indicate adjusted $p < 0.05$ by Tukey's HSD test.

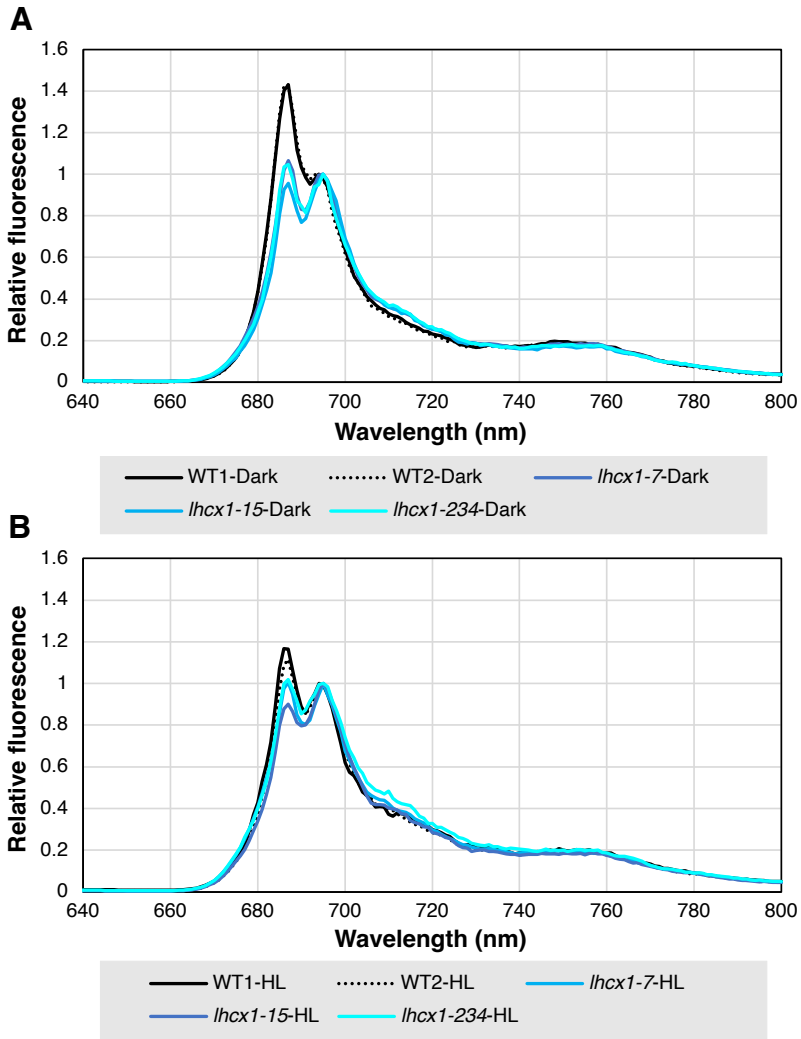

Figure 5. Low-Temperature Fluorescence Emission Spectra of Wild-Type (WT) and *lhcx1* Mutants Cultured Under High Light

A) Low-temperature fluorescence emission spectra measured after 30 minutes of dark treatment followed by rapid freezing in liquid nitrogen. B) Low-temperature fluorescence emission spectra measured after 30 minutes of HL treatment followed by rapid freezing in liquid nitrogen. Each spectrum was normalized at the peak corresponding to CP47 (693–695 nm). The wild type was measured in two separately cultured samples (black solid line and black dashed line).

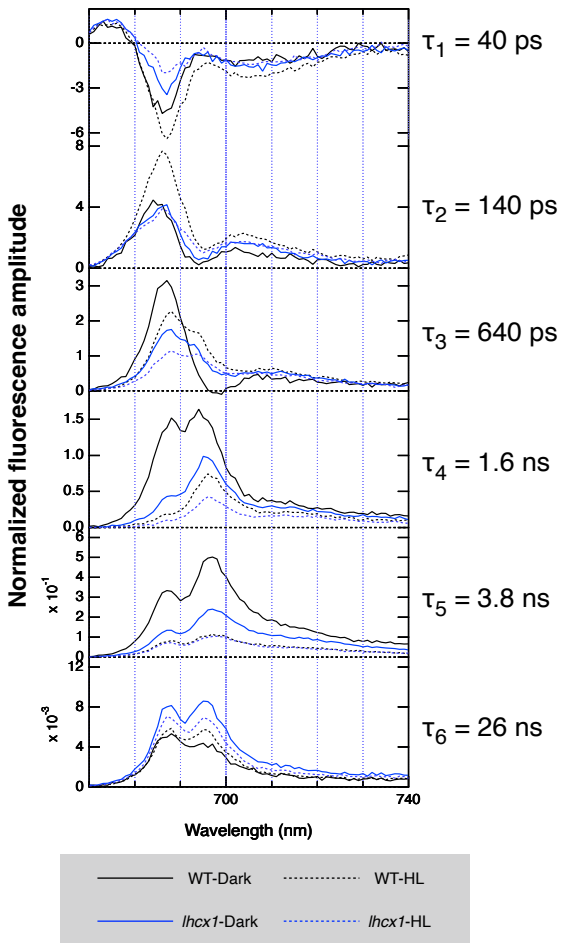

1089 **Figure 6. Fluorescence Decay-Associated Spectra of Time-Resolved Fluorescence**

1090 Black lines indicate WT, blue lines indicate *lhcx1-7*, solid lines represent measurements after 30

1091 minutes of dark treatment, and dashed lines represent measurements after 30 minutes of treatment at

1092 300 µmol photons m^{-2} s^{-1}.

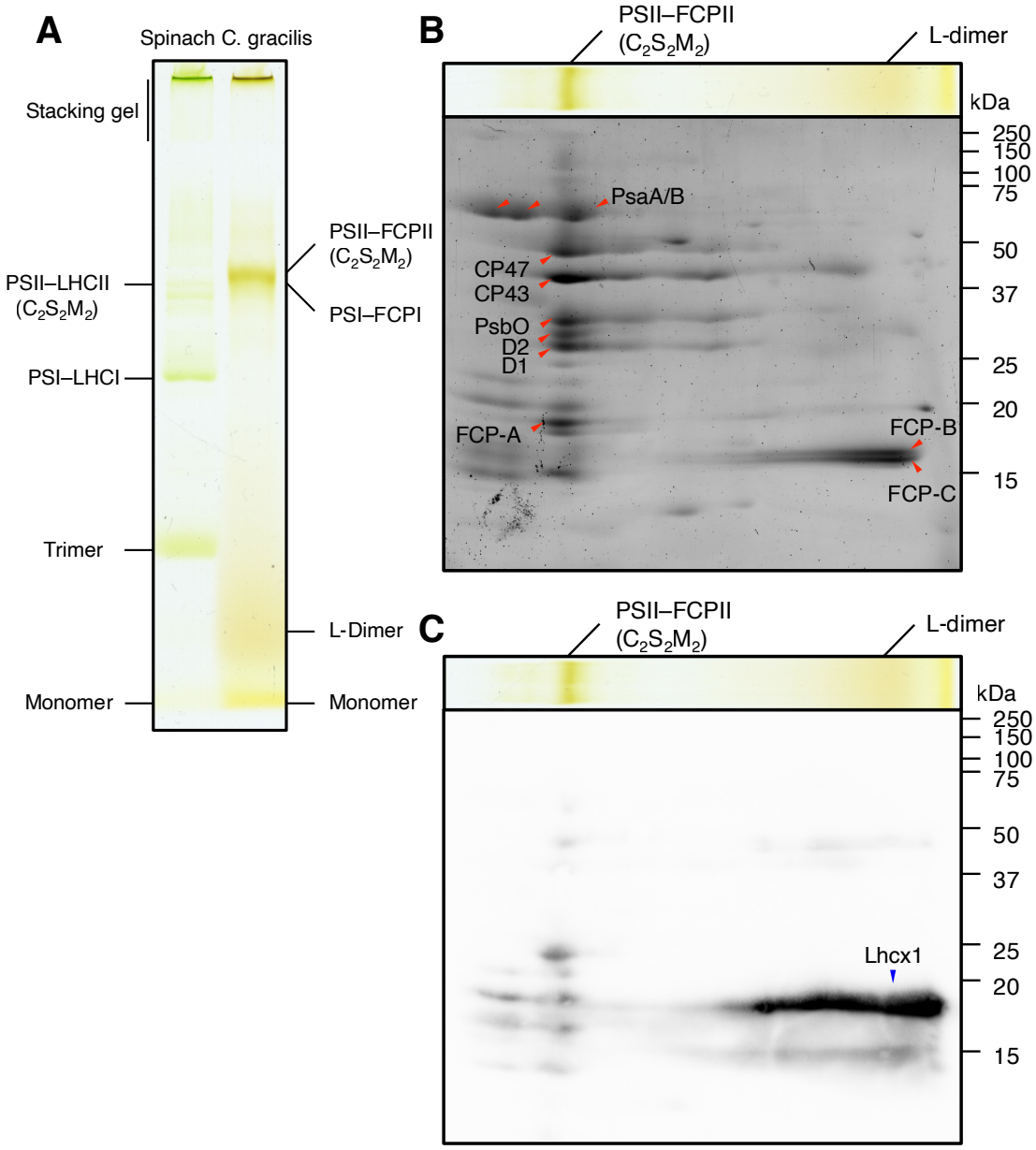

Figure 7. 2D-Amphipol-based-CN/SDS-PAGE of *C. gracilis* Thylakoid Membranes

A) Amphipol-based CN-PAGE of *C. gracilis* and spinach thylakoid membranes. Annotation of each band for spinach follows previous reports (Järvi et al., 2011; Kameo et al., 2021). B) Protein fluorescence staining image of two-dimensional electrophoresis of Amphipol-based CN-PAGE. Annotation of each spot indicated by red arrowheads is based on previous reports (Nagao et al., 2007).

1099 FCP-A, FCP-B, and FCP-C correspond to CgLhcf1, CgLhcf12, and CgLhcf2, respectively (Nagao et

1100 al., 2019; Nagao et al., 2022; Zhou et al., 2024). C) Identification of the Lhcx1 spot by immunoblotting

1101 using anti-Lhcx1 antibody. The blue arrowhead indicates the detected spot.

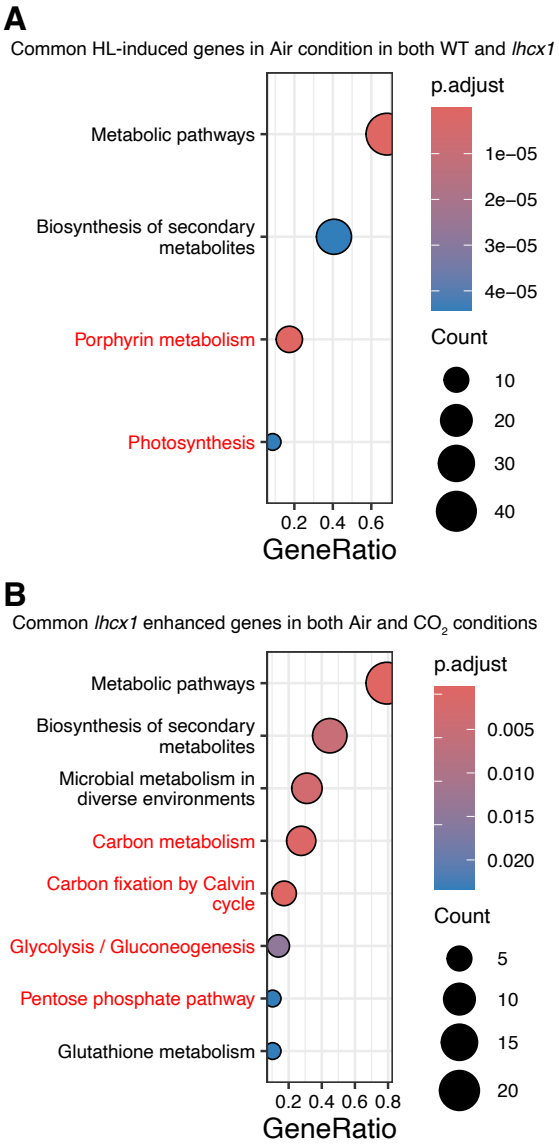

Figure 8. Gene Expression Analysis under CO_2 Enrichment

KEGG pathway enrichment analysis of differentially expressed genes in the *lhcx1* mutant under LL and HL conditions. A**)** Pathways enriched in genes commonly induced by HL in both WT and the *lhcx1* mutant under ambient air conditions. B**)** Pathways enriched in genes showing enhanced HL response in *lhcx1* mutant under both ambient air and CO_2-enriched conditions. Dot size represents gene count, and color intensity indicates statistical significance (q-value shown as p.adjust). Pathways related to typical HL response and photosynthesis are indicated with red letters.

Supplemental Figures and Data

Supplemental Figure 1. Generation of hCas9-Expressing Host Strain

Supplemental Figure 2. Confirmation of Lhcx1 Deficiency in *lhcx1* Genome-Edited Strains

Supplemental Figure 3. Growth Curves of *C. gracilis* Wild-Type and *lhcx1* Strains Cultured with Aeration for 7 Days Under High Light

Supplemental Figure 4. PAM Fluorescence Measurements of *C. gracilis* Wild-Type and *lhcx1* Strains Cultured with Aeration for 3 Days Under Low Light (LL) and High Light (HL)

Supplemental Figure 5. Total Absorption Spectra of Low Light (LL, left) and High Light (HL, right) Cultures

Supplemental Figure 6. Relative PSII Antenna Size of Wild-Type (WT) and *lhcx1* Mutants

Supplemental Figure 7. Fluorescence Decay-Associated Spectra of Time-Resolved Fluorescence of *lhcx1-15*, *lhcx1-234*, and the second replicate of WT

Supplemental Figure 8. Amphipol-based-CN-PAGE of Thylakoid Membranes of *C. gracilis* WT and *lhcx1* Mutants

Supplemental Figure 9. PAM Fluorescence Measurements of *C. gracilis* Wild-Type and *lhcx1* Strains Cultured with 3% CO_2 Aeration for three Days Under Low Light (LL) and High Light (HL)

Supplemental Figure 10. TPM of *CgLhcx1–3*.

Supplemental Data 1. Comprehensive RNA-Seq gene expression data including normalized expression values (TPM, FPKM), differential expression statistics (Log2FC, p-value, FDR), and gene annotations for all detected genes across four experimental conditions.